

Key Points:

- Longitude-latitude maps of the thermal inertia and dielectric constant of asteroid (16) Psyche derived from Atacama Large Millimeter Array data
- The surface of Psyche is heterogeneous and shows signatures suggestive of both metal- and silicate-rich materials
- A depression on Psyche with distinctive thermal-inertia properties suggests an evolved surface processed by impacts

Supporting Information:

Supporting Information may be found in the online version of this article.

Correspondence to:

S. Cambioni,
cambioni@mit.edu

Citation:

Cambioni, S., de Kleer, K., & Shepard, M. (2022). The heterogeneous surface of asteroid (16) Psyche. *Journal of Geophysical Research: Planets*, 127, e2021JE007091. <https://doi.org/10.1029/2021JE007091>

Received 18 OCT 2021

Accepted 13 MAY 2022

Author Contributions:

Conceptualization: Saverio Cambioni

Data curation: Katherine de Kleer

Formal analysis: Saverio Cambioni,

Katherine de Kleer, Michael Shepard

Funding acquisition: Saverio Cambioni,

Katherine de Kleer

Investigation: Saverio Cambioni,

Katherine de Kleer, Michael Shepard

Methodology: Saverio Cambioni

Software: Saverio Cambioni

Supervision: Katherine de Kleer

Writing – original draft: Saverio Cambioni,

Katherine de Kleer, Michael Shepard

© 2022 The Authors.

This is an open access article under the terms of the [Creative Commons Attribution-NonCommercial License](https://creativecommons.org/licenses/by-nc/4.0/), which permits use, distribution and reproduction in any medium, provided the original work is properly cited and is not used for commercial purposes.

The Heterogeneous Surface of Asteroid (16) Psyche

Saverio Cambioni¹ , Katherine de Kleer² , and Michael Shepard³ 

¹Department of Earth, Atmospheric & Planetary Sciences, Massachusetts Institute of Technology, Cambridge, MA, USA,

²Division of Geological & Planetary Sciences, California Institute of Technology, Pasadena, CA, USA, ³Department of Environmental, Geographical & Geological Sciences, Bloomsburg University, Bloomsburg, PA, USA

Abstract Main-belt asteroid (16) Psyche is the largest M-type asteroid, a class of object classically thought to be the metal cores of differentiated planetesimals and the parent bodies of the iron meteorites. de Kleer, Cambioni, and Shepard (2021, <https://doi.org/10.3847/psj/ac01ec>) presented new data from the Atacama Large Millimeter Array (ALMA), from which they derived a global best-fit thermal inertia and dielectric constant for Psyche, proxies for regolith particle size, porosity, and/or metal content, and observed thermal anomalies that could not be explained by surface albedo variations only. Motivated by this, here we fit a model to the same ALMA data set that allows dielectric constant and thermal inertia to vary across the surface. We find that Psyche has a heterogeneous surface in both dielectric constant and thermal inertia but, intriguingly, we do not observe a direct correlation between these two properties over the surface. We explain the heterogeneity in dielectric constant as being due to variations in the relative abundance of metal and silicates. Furthermore, we observe that the lowlands of a large depression in Psyche's shape have distinctly lower thermal inertia than the surrounding highlands. We propose that the latter could be explained by a thin mantle of fine regolith, fractured bedrock, and/or implanted silicate-rich materials covering an otherwise metal-rich surface. All these scenarios are indicative of a collisionally evolved world.

Plain Language Summary Asteroid (16) Psyche is the target of the eponymous NASA mission, which will assess whether the asteroid is the exposed core of an early pre-planet. The Atacama Large (Sub-) Millimeter Array located on the Chajnantor Plateau in Chile allowed the acquisition of temperature images of Psyche at a resolution of 30 km/pixel (the highest ever achieved from Earth). We analyze these images to map the metal content of the first millimeters of the surface as function of longitude and latitude. We find that the relative abundance of metals and silicates varies across the surface. Additionally, we observe that the lowlands of a large depression change temperature much faster than the surrounding highlands as Psyche rotates on its spin axis. Based on this, we propose that the lowlands could exhibit ponds of fine-grained materials, be highly fractured, and/or host silicate-rich materials implanted by impacts. All these scenarios are indicative of an evolved surface processed by impacts.

1. Introduction

The upcoming NASA Psyche mission will explore main-belt asteroid (16) Psyche (henceforth just “Psyche”), an M-type asteroid of about 220 km in size which could have been part of a differentiated planetesimal (Elkins-Tanton et al., 2022). Planetesimals are thought to be born 100 km in size and larger (e.g., Morbidelli et al., 2009). During the evolution of the solar system, some may have survived relatively intact, while others suffered collisions and created asteroid families (e.g., Delbo’ et al., 2017), and others may have lost their mantle materials with no apparent associated family (Davis et al., 1999). Psyche could be a differentiated planetesimal that lost its mantle in a hit-and-run collision (e.g., Asphaug & Reufer, 2014), a rubble pile of material that was previously part of a differentiated body, or a primitive object of unusually metal-rich composition. Answering the question “what is Psyche?” is valuable for constraining the collisional evolution of the planetesimals and requires linking remote sensing observations of their surfaces to the properties of their interiors.

The M-type asteroids (Tholen, 1984) are a diverse group (Table 1), which is broken down in the Bus–DeMeo taxonomy into the Xc class, associated with enstatite chondrites, and the Xk class, associated with mesosiderites (DeMeo et al., 2009). Neeley et al. (2014) compared the optical-near-infrared spectra for 29 M-type asteroids to meteorites and found that, while the best analog types are iron meteorites in most cases, 21% of the targets were better fit by enstatite chondrites, consistent with early studies (e.g., Chapman & Salisbury, 1973; Vernazza et al., 2009). Insights into the concentration of metal in the near-surface of asteroids come from measurement

Table 1
Properties of Some M-Type Asteroids

Asteroid	a [AU]	D [km]	Radar albedo	Γ [tiu]	Analog?	3- μ m?	References
16 Psyche	2.92	222^{+4}_{-1}	0.34 ± 0.08	280 ± 100	see text	yes	S21; DK21; T17
21 Lutetia	2.44	98 ± 2	0.24 ± 0.07	20–30	EC	yes	S15; C11; S10; R11
22 Kalliope	2.91	168 ± 3	0.18 ± 0.05	125 ± 125	IM + PYR	yes	S15; M12; F10; OB10
55 Pandora	2.76	85 ± 3	-	-	IM	yes	OB10
69 Hesperia	2.98	136 ± 14	0.45 ± 0.12	-	IM + PYR	yes	S15; H05; L15
77 Frigga	2.67	61.4 ± 0.2	0.14 ± 0.04	-	-	-	S15
92 Undina	3.19	108 ± 5	0.38 ± 0.09	-	IM + PYR	yes	S15; F11; R00
97 Klotho	2.67	88 ± 24	0.26 ± 0.05	-	EC, CH	no	S15; S10; OB10
110 Lydia	2.73	88 ± 3	0.37 ± 0.10	135 ± 65	IM + PYR	yes	S15; DT09; H05; OB10
125 Liberatrix	2.74	48.4 ± 0.5	-	71^{+26}_{-24}	IM + PYR	no	ME21; H05; R00
129 Antigone	2.87	128.7 ± 0.6	0.36 ± 0.09	-	CB?	yes	S15; S10; OB10
135 Hertha	2.43	71 ± 3	0.18 ± 0.05	-	CH, EC	yes	S15; S10; OB10
136 Austria	2.29	36.9 ± 0.5	-	-	-	yes	L15
201 Penelope	2.68	86 ± 3	0.40 ± 0.10	<50	IM + PYR	yes	S15; M05; H05; R00
216 Kleopatra	2.79	119 ± 3	0.43 ± 0.10	>50	IM + PYR	no	S18; M05; OB10; L15
224 Oceana	2.65	58.2 ± 0.8	0.25 ± 0.10	-	EC, CH	-	S15; S10
250 Bettina	3.15	121 ± 2	-	-	IM + PYR	-	OB10; H07
347 Pariana	2.61	48.6 ± 0.1	0.36 ± 0.09	-	IM, CB	-	S15; S10
382 Dodona	3.12	65.2 ± 0.5	-	60^{+90}_{-45}	IM + PYR	-	ME21; H11
413 Edburga	2.58	25 ± 5	0.35 ± 0.09	100^{+60}_{-60}	IM, EC	no	S15; ME21; H07; R00
441 Bathilde	2.81	66 ± 2	0.20 ± 0.05	180^{+20}_{-60}	-	-	S15; PG19
497 Iva	2.85	40.9 ± 0.3	0.24 ± 0.08	70^{+19}_{-25}	SIM, CH	no	S15; ME21; OB10; OB10
766 Moguntia	3.02	41.0 ± 0.1	-	-	IM + OLI	-	H11
785 Zwetana	2.57	49 ± 1	0.26 ± 0.07	<50	IM, CB	no	S15; M05; OB10; OB10
798 Ruth	3.01	46 ± 7	-	-	IM + OLI	-	H11
1210 Morosovia	3.01	33.7 ± 0.3	-	-	IM + OLI	-	H11

Note. “a” is the semi-major axis of the asteroid in Astronomical Units (AU). D is the mean or effective diameter, latest WISE value from Masiero et al. (2011, 2012, 2014, 2021) as listed in the Minor Planet Physical Properties Catalog (MP3C, <https://mp3c.oca.eu/>), except for Psyche (21) Lutetia, and (69) Hesperia and (798) Ruth, for which the values are from Shepard et al. (2021), Sierks et al. (2011), and Alí-Lagoa et al. (2018), respectively. The MP3C, developed and maintained at the Observatoire de la Côte d’Azur, is a Service National d’Observation (SNO) of Institut des Sciences de l’Univers (INSU), CNRS. Γ is thermal inertia, that is, the resistance of surface material to change temperature. Uncertainties are 1-Standard Deviation. IM = Iron Meteorites; EC = Enstatite Chondrites; CB = High-Iron Carbonaceous Chondrites; CH = CH Meteorites; SIM = Stony-Iron Meteorites. The acronyms PYR and OLI indicate the detection of pyroxene- and olivine-bands in the bodies’ spectra. References for radar albedo, thermal inertia, silicates and OH/H₂O band are listed using the following acronyms: C11: Coradini et al. (2011); DK21: de Kleer, Cambioni, and Shepard (2021); DT09: Delbo’ and Tanga (2009); F10: Fornasier et al. (2010); F11: Fornasier et al. (2011); H05: Hardersen et al. (2005); H07: Hardersen et al. (2007); H11: Hardersen et al. (2011); L15: Landsman et al. (2015); M05: Mueller et al. (2005); M12: Marchis et al. (2012); ME21: MacLennan and Emery (2021); OB10: Ockert-Bell et al. (2010); PG19: Podlowska-Gaca et al. (2020) R11: Rivkin et al. (2011); S10: Shepard et al. (2010); S15: Shepard et al. (2015); S18: Shepard et al. (2018); S21: Shepard et al. (2021); T17: Takir et al. (2017).

of radar echoes, in which a circularly polarized continuous wave signal is transmitted to the asteroid and the echo power in the same (SC) and opposite (OC) senses of polarization is measured. The OC radar albedo (henceforth just “radar albedo”) is the ratio of the power received from target asteroids relative to that which would be measured from a metallic sphere of the same cross-sectional area and at the same distance. Radar albedo increases with increasing metal content of the near-surface material (e.g., Shepard et al., 2015). The average radar albedo of the M-type group is 0.28 ± 0.13 (Shepard et al., 2010, 2021), which is much higher than that of S-type or C-type asteroids (~ 0.14 , e.g., Magri et al., 2007) and, as such, indicative of a higher metallic content of the surface material (Ostro et al., 1985). Another proxy for surface metal content is the thermal inertia Γ ,

which is the resistance of the surface material to change temperature during the diurnal illumination cycle. Γ is a composite parameter function of the material thermal conductivity κ , specific heat capacity c_p , and bulk density ρ of the surface ($\Gamma = \sqrt{\kappa c_p \rho}$). Thermal inertia Γ is measured in units of $\text{J m}^{-2} \text{K}^{-1} \text{s}^{-0.5}$, which will hereafter be referred to as “tiu” for “thermal inertia unit.” For a given particle size, metal-rich regolith tends to have higher thermal inertia than silicate-rich ones (Matter et al., 2013); consistently, some M-type asteroids appear to have higher thermal inertia than similar-sized C-type or S-type asteroids (e.g., Delbo et al., 2015). However, evidence for a correlation between thermal inertia and radar albedo among M-type asteroids is marginal to none (Table 1; see also Landsman et al., 2019; Elkins-Tanton et al., 2020).

Spectroscopic observations of M-type asteroids also revealed the presence of silicate features in otherwise featureless iron-meteorite-like spectra (e.g., Fornasier et al., 2010; Hardersen et al., 2005). This material may be what remains of stripped rocky mantles, supporting the hypothesis that M-type asteroids are the cores of differentiated planetesimals (e.g., Asphaug & Reufer, 2014; Bell et al., 1989; Scott et al., 2015). At the low pressures of planetesimals' magma oceans, olivine is expected to be the first mineral to crystallize across a vast range of possible bulk compositions (Elkins-Tanton et al., 2013; Elkins-Tanton & Weiss, 2017). Although the spectroscopic signature of olivine was observed on M-type asteroids (766) Moguntia, (798) Ruth and (1210) Morosovia (Hardersen et al., 2011), the near-infrared spectra of many other M-type asteroids, such as Psyche, (22) Kalliope, (69) Hesperia, (110) Lydia and (201) Penelope were found to show only a weak absorption feature near $0.93 \mu\text{m}$ indicative of low-Fe, low-Ca pyroxene (B. E. Clark et al., 2004; Hardersen et al., 2005; Fornasier et al., 2010; Birlan et al., 2007; Sanchez et al., 2017). Pyroxenes may form through reduction of olivine in a low oxygen fugacity environment, such as that of the nebular region close to the Sun or in a forming planetary core (Elkins-Tanton et al., 2013; Hardersen et al., 2005). The dominance of one mineralogy over the other in the M-type population could be indicative of where the asteroids accreted or how they differentiated (Hardersen et al., 2005).

The third component detected on the surfaces of M-type asteroids is hydrated minerals (e.g., Rivkin et al., 2000; Shepard et al., 2015; Takir et al., 2017). If hydrated minerals are endogenic to M-types, this would suggest that they accreted beyond the water-ice condensation line of the early solar system (Elkins-Tanton et al., 2022; Landsman et al., 2015). Another explanation is that the hydrated material is exogenic (Avdellidou et al., 2018; Busarev, 2002; Shepard et al., 2015), consistent with predictions of low volatile content in silicate magmas on planetesimals (Weiss & Elkins-Tanton, 2013) and with spacecraft observations of implanted exogenic material on asteroids of sizes ranging from 500-km-sized (4) Vesta to sub-km-sized (101955) Bennu (Reddy et al., 2012; DellaGiustina et al., 2021). Another possible explanation is that space weathering of M-type asteroids' surface material may produce hydrated minerals via interaction of solar wind protons with oxygen-bearing minerals (Landsman et al., 2015), as was proposed for the Moon (e.g., R. N. Clark, 2009; Sunshine et al., 2009; Pieters et al., 2009); although, more laboratory experiments are needed to test this proposal specifically for M-types.

1.1. This Work

On Psyche, variations in metal and silicate content have been proposed on the basis of rotational variations of the surface at visible, infrared and radar wavelengths (Ferrais et al., 2020; Hardersen et al., 2005; Sanchez et al., 2017; Shepard et al., 2021; Takir et al., 2017; Viikinkoski et al., 2018). de Kleer, Cambioni, and Shepard (2021) observed Psyche in thermal emission using the Atacama Large (Sub-)Millimeter Array (ALMA) at a resolution of 30 km over 2/3 of its rotation and fit for the thermal inertia and dielectric constant (i.e., the polarizability of the surface material, to be presented in Section 2.2) with a single value of each property over the entire surface. Their results showed the presence of thermal anomalies which support the heterogeneity of surface composition and could not be explained by surface albedo variations only. Motivated by this, here we fit a model to the same ALMA data set that allows thermal inertia and dielectric constant to vary across the surface. We describe the methodology in Section 2. In Section 3, we present the results as longitude-latitude maps of surface properties and test their robustness to model assumptions. In Section 4, we discuss possible metal-rich and metal-poor areas on the basis of dielectric constant measurements and discuss a prominent feature in the thermal inertia map.

2. Materials and Methods

2.1. Data

The data analyzed in this paper were obtained at ALMA on 2019 June 19 between 06:33 and 09:11 UT. The observations, data reduction, and imaging methods are described in de Kleer, Cambioni, and Shepard (2021) and are only briefly summarized here. Data were obtained at a wavelength of 1.3 mm over 8 GHz of total bandwidth, all of which was used in the analysis. The maximum baseline at the time of observation was 16.2 km, and Psyche was at a distance of 2.04 AU from Earth (and 2.78 AU from the Sun) resulting in a spatial resolution of ~ 30 km on Psyche, or an angular resolution of ~ 0.02 . The sub-observer and sub-solar latitudes on Psyche at the time of observation were -14° and 3° respectively, and the solar phase angle was 17° . Rotation curves of the total flux density and peak brightness temperature for the ALMA observations are in figure 2 of de Kleer, Cambioni, and Shepard (2021). The data were reduced and calibrated by the ALMA pipeline, and were further calibrated and imaged using the Common Astronomy Software Applications (CASA) package (McMullin et al., 2007). The duration of each ALMA scan of Psyche was under 1 min, and several scans were imaged together to improve the signal-to-noise. Loss of resolution from smearing was avoided by keeping the observing interval of jointly imaged scans below 6 min. Each final image has a signal-to-noise of ~ 45 – 50 and a noise level around 2.5 K.

2.2. Choice of Model Parameters

Measurements of thermal emission of asteroids provide constraints on the particle size, porosity, and/or metal content of the surface materials. Thermal observations from Earth have been typically acquired in infrared wavelengths and interpreted using thermophysical models (e.g., Delbo et al., 2015) for which the free parameters are the thermal inertia Γ (defined in Section 1) and the roughness of the surface f . The latter measures the root-mean-square slope of topography that has spatial scales below the resolution of the shape model of the asteroid. A rougher surface has higher mean surface slope and stays warmer for longer periods of time than it would if it were smoother due to higher absorption of sunlight and more self-heating (e.g., Delbo et al., 2015; Rozitis, 2017). Different approaches to model surface roughness exist in literature (Delbo et al., 2015). The thermophysical model we use here (to be presented in Section 2.3) allows for modeling of surface roughness by carving one spherical craters onto each facet of the shape model and tune the root-mean-square slope f of the facets by either changing the opening angle or the areal fractional coverage of the craters, or both.

Mid-infrared observations do not currently resolve the thermal emission from the surface of Psyche because the high required angular resolution ($\sim 0.03''$) is beyond the capabilities of existing facilities. Alternatively, de Kleer, Cambioni, and Shepard (2021) used ALMA to acquire thermal emission maps of Psyche at a resolution of 30 km/pixel. ALMA is an astronomical interferometer composed of 66 antennas distributed in the Chajnantor plateau in Chile. The antennas observed Psyche's thermal emission at millimeter wavelengths and combined the signals interferometrically into a synthetic signal equivalent to that observed by a putative telescope with an effective diameter of 16 km. The foundational theory of how to analyze thermal emission of solar system bodies at millimeter wavelengths can be found in numerous investigations of the Moon (e.g., Muhleman, 1972; Piddington & Minnett, 1949; Ulich et al., 1974; Zheng et al., 2019), dwarf planet Ceres (W. J. Webster et al., 1988; Webster et al., 1989; Redman et al., 1998; Altenhoff et al., 1994; Li et al., 2020), asteroids (3) Juno (ALMA Partnership et al., 2015; Altenhoff et al., 1994), Vesta (e.g., Webster et al., 1989; Altenhoff et al., 1994), Psyche (de Kleer, Cambioni, & Shepard, 2021), (21) Lutetia (Gulkis et al., 2012) and (2867) Steins (Gulkis et al., 2010), and of icy solar system bodies (de Kleer, Butler, de Pater et al., 2021; Lellouch et al., 2017; Muhleman & Berge, 1991; Trumbo et al., 2018). Discussion of issues related to physical propagation of thermal emission at different wavelengths can be found in Lagerros (1996); Redman et al. (1998); S. J. Keihm (1982); S. Keihm et al. (2013); Hayne et al. (2017), and in de Kleer, Butler, Cordiner, et al. (2021) for the specific case of solar system science with ALMA.

At millimeter wavelengths, the thermal emission of the surface (or, equivalently, its brightness temperature) is sensitive to the complex dielectric constant ϵ of the near surface material and the temperature profile within the (sub)surface. The dielectric constant measures the polarizability of the surface material, has real part ϵ' and imaginary part ϵ'' (as such, $\epsilon = \epsilon' + i\epsilon''$) and is equal to \tilde{n}^2 , where $\tilde{n} = n + iK$ is the complex refractive index. n is the ratio of the speed of light in a vacuum to the speed of light in the material and K is the extinction coefficient measuring the amount of attenuation when the electromagnetic wave propagates through the material. The

extinction coefficient defines the electrical skin depth $\delta_{elec} = \lambda/(4\pi K)$ within which the emission is reduced by $1/e$ assuming a non-conducting material for emission at wavelength λ . While this depth is small at infrared wavelengths, it becomes significant at longer wavelengths, hence the need to integrate the thermal emission within the subsurface (e.g., Gulkis et al., 2010) for a temperature profile as a function of thermal inertia Γ and surface roughness f . Since \bar{n} defines the reflection coefficients of the surface, the millimeter emissivity of the surface E , that is, the degree of emission relative to a blackbody, is a decreasing function of dielectric constant. For low-emissivity asteroids like Psyche (global $E = 0.4$ – 0.7 , de Kleer, Cambioni, & Shepard, 2021), thermal emission at millimeter wavelengths is particularly sensitive to metal content and porosity of the surface material (see their Section 3.5.3).

2.3. Thermal Emission Images

To interpret the ALMA observations, we generate thermal emission images at the same viewing geometry and wavelength of the ALMA data with thermal inertia and dielectric constant as free parameters. The thermophysical simulation setup and the methodology to create model images are the same of de Kleer, Cambioni, and Shepard (2021), with a few adaptations as described in the following.

We use a well-established ThermoPhysical Model (Delbo et al., 2015) to solve the non-dimensionalized 1-D heat conduction equation with thermal inertia Γ as free parameter. We explore the following values of thermal inertia: $\Gamma = (25, 75, 116, 135, 156, 181, 210, 283, 442, 594, 1000)$ tiu . We assume surface roughness $f = 0^\circ$ (i.e., a smooth surface) as this was found to best-fit the thermal emission data at both infrared (Landsman et al., 2018; Matter et al., 2013) and mm-wavelengths (de Kleer, Cambioni, & Shepard, 2021). We assume bolometric emissivity $E_{bol} = 0.9$, bond albedo $A = 0.05$, and asteroid topography as defined by the shape model by Shepard et al. (2021). We test the robustness of the results against the assumption that the facets of the shape model are smooth and the entire surface has the same Bond albedo in Section 3.4.

Next, we compute the blackbody flux density for the facets of the shape model based on the temperature output of the TPM. For each facet of the shape model, the TPM computes the temperature as a function of dimensionless depth parameter $x' = x/\delta_{th}$, where x is the depth in physical units and δ_{th} is the diurnal thermal skin depth over which the amplitude of the diurnal temperature wave is reduced by $1/e$:

$$\delta_{th} = \sqrt{\frac{P}{\pi}} \frac{\Gamma}{\rho c_p} \quad (1)$$

with rotation period $P = 4.195,948$ hr for Psyche (Shepard et al., 2021). For each value of Γ , we compute the corresponding δ_{th} assuming a bulk density $\rho = 3500$ kg/m^3 which was derived from Psyche's radar albedo of 0.34 ± 0.08 by Shepard et al. (2021) and a value of specific heat $c_p = 370$ J/kg K . The latter is an average value of possible meteorite analogs for Psyche identified by Elkins-Tanton et al. (2020): mesosiderites ($c_p = 383 \pm 6$ J/kg K), iron IIAB ($c_p = 342 \pm 6$ J/kg K) and iron IIIAB ($c_p = 375 \pm 23$ J/kg K) computed at ~ 200 K (Consolmagno & Britt, 2013; Consolmagno et al., 2013). We convert the dimensionless depth parameter x' to physical units and calculate the temperature as a function of physical depth. We use Equation 3 from de Kleer, Butler, de Pater et al. (2021) to integrate the blackbody flux density through the subsurface along the viewing path. The integration along the viewing path depends on the dielectric constant ϵ . Because $K^2/\epsilon' < 0.006$ for most meteorites (Campbell & Ulrichs, 1969), hereafter we make the simplification that $\epsilon = \epsilon'$ as in de Kleer, Cambioni, and Shepard (2021). We explore the following values of ϵ : (3.0, 7.5, 12.0, 16.5, 17.5, 18.5, 19.5, 20.5, 21.5, 25.5, 30.0, 55.0, 80.0). This array is more finely sampled around the best-fit $\epsilon = 18.5$ found by de Kleer, Cambioni, and Shepard (2021). We discuss the range of applicability of the results based on the assumed bulk density value in Section 4.1.

Next, we correct the thermal emission from each facet for the millimeter emissivity E of the surface material. The emissivity as a function of emission angle is computed using the Fresnel reflection coefficients for polarization parallel and perpendicular to the direction of propagation, which in turn depend on the complex refractive index (see Equation 9 in de Kleer, Cambioni, & Shepard, 2021) and thus on the dielectric constant of the material (Section 2.2). We explore the same array of values of dielectric constant as described above.

Next, we obtain model thermal-emission images for Psyche by projecting the shape model by Shepard et al. (2021) onto the plane-of-sky in the International Celestial Reference System (ICRS), which is that of the

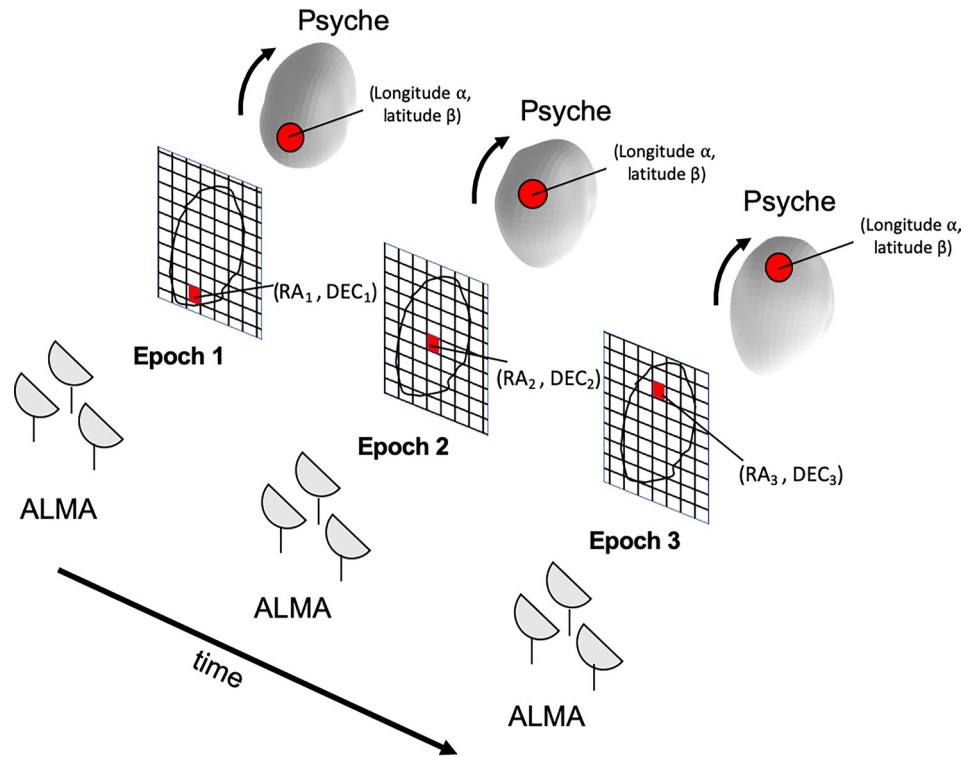


Figure 1. As the asteroid rotates during the observation epochs, the same facet of longitude α and latitude β is seen at different right ascensions R.A. and declinations decl. in the Atacama Large Millimeter Array (ALMA) images. We use the knowledge of the (R.A., decl.) of the projected facets and the (R.A., decl.) of the ALMA pixels to associate a thermal-emission curve to each facet. We then fit modeled thermal emission curves corresponding to different values of thermal inertia and dielectric constant to the observed thermal emission curves.

ALMA observations. We illustrate the projection of the surface areas onto the R.A. and decl. observed by ALMA in Figure 1. The vertices of the facets are arrays defined in the asteroid reference system, which has positive \hat{x} axis along the direction of the prime meridian (PM) as defined by Shepard et al. (2021), positive \hat{z} axis in the direction of the rotation pole, and the third axis to complete the orthonormal frame. We rotate the vertices to ICRS as described on the DAMIT website (<https://astro.troja.mff.cuni.cz/projects/damit/pages/documentation>):

$$r_{ICRS} = R_x(\theta_3) R_z(\theta_1) R_y(90 - \theta_2) R_z\left(\phi_0 + \frac{2\pi}{P}(t - t_0)\right) r_{ast} \quad (2)$$

where $\theta_1 = 36^\circ$ and $\theta_2 = -8^\circ$ are the longitude and latitude of the asteroid spin axis, $\phi_0 = 341.56^\circ$ is the initial rotation angle of the asteroid, t is the observation epoch, t_0 is J2000, and $\theta_3 = 23.44^\circ$ is the Earth's obliquity. The matrices R_x , R_y and R_z are defined, for a generic angle θ , as:

$$R_x(\theta) = \begin{bmatrix} 1 & 0 & 0 \\ 0 & \cos \theta & -\sin \theta \\ 0 & \sin \theta & \cos \theta \end{bmatrix}, R_y(\theta) = \begin{bmatrix} \cos \theta & 0 & \sin \theta \\ 0 & 1 & 0 \\ -\sin \theta & 0 & \cos \theta \end{bmatrix}, R_z(\theta) = \begin{bmatrix} \cos \theta & -\sin \theta & 0 \\ \sin \theta & \cos \theta & 0 \\ 0 & 0 & 1 \end{bmatrix} \quad (3)$$

Next, we interpolate the thermal emission values of the projected facets that are visible to ALMA in R.A. and decl. to produce a 2D array whose pixels correspond to those of the ALMA images. Finally, the model images are convolved with the ALMA beam to model the observation conditions. The above procedure is used to build a look-up table of images for every combination of the values of thermal inertia Γ and dielectric constant ϵ listed above.

2.4. Fitting Γ and ϵ to the Thermal-Emission Curves

Our goal is to fit a value of thermal inertia and a value of dielectric constant to the ALMA images for each surface area, and see whether this can explain the residuals from the best-fit global model by de Kleer, Cambioni, and Shepard (2021), who determined a global best-fit value of thermal inertia and dielectric constant for the entire surface to the data. Here the term “surface area” indicates the ensemble of projected facets of the shape model that are imaged in different ALMA pixels as the asteroid rotates and the surface area moves across the plane of sky. We apply the procedure of Section 2.3 to the data to determine the R.A. and decl. of the projected facets that are visible at a given observing epoch and associate thermal-emission values to such facets based on the corresponding ALMA pixels. The thermal emission curve \mathbf{D} of a surface area is the variation in thermal emission as a function of time as the asteroid rotates and a facet moves across the plane of sky. We repeat the same procedure to generate model thermal-emission curves $\mathbf{M}(\Gamma, \epsilon)$ for each facet as a function of thermal inertia Γ and dielectric constant ϵ . We evaluate the goodness-of-fit of each modeled thermal emission curve $\mathbf{M}(\Gamma, \epsilon)$ for a given thermal inertia Γ and dielectric constant ϵ by evaluating its χ_r^2 (reduced chi-square) function (e.g., Hanuš et al., 2015):

$$\chi_r^2(\Gamma, \epsilon) = \frac{1}{N_{obs} - 2} \sum_{i=1}^{N_{obs}} \frac{(\mathbf{M}^i(\Gamma, \epsilon) - \mathbf{D}^i)^2}{\sigma_D^2}, \quad (4)$$

where σ_D is the image background noise (Section 2.1) and $N_{obs} \leq 22$ is the number of times the projected facet was observed by ALMA. The set \mathbf{S} of values of thermal inertia and dielectric constant that best fit the thermal emission curve \mathbf{D} are found by taking the median of the (Γ, ϵ) whose $\chi_r^2(\Gamma, \epsilon)$ values meet the following criterion:

$$(\Gamma, \epsilon) \in \mathbf{S} \quad \text{if} \quad \chi_r^2(\Gamma, \epsilon) < \min_{\chi_r^2} \times \left(1 + \sqrt{\frac{2}{N_{obs} - 2}} \right). \quad (5)$$

We consider the median to be a more reliable estimator of the central tendency of \mathbf{S} than the minimum of the χ_r^2 , which is not distinguishable from other solutions in \mathbf{S} in virtue of Equation 5, the mean of \mathbf{S} , which is more sensitive to outliers than the median, and the mode of \mathbf{S} , which is not sensitive to elements in the set different from the most recurrent ones. We compute the uncertainty of the best-fit values of (Γ, ϵ) as the standard deviation of the solutions in \mathbf{S} .

2.5. Mapping (Γ, ϵ) in Longitude and Latitude

We display the best-fit (Γ, ϵ) and uncertainties as function of asteroid-centric longitude α and latitude β using the Mollweide (equal-area, pseudocylindrical) cartographic map projection technique with the prime meridian (PM) at the center of the map. To take into account the correlation between nearby pixels that characterizes the ALMA images (i.e., each ALMA beam contains about 45 pixels, de Kleer, Cambioni, & Shepard, 2021), we bin the surface properties in longitude and latitude on a grid with elements of angular size $5^\circ \times 5^\circ$ and apply Gouraud shading (Gouraud, 1971). We hatch the region between longitudes 60°W and 120°W to indicate that the solution for that region could be affected by model artifacts. The region was observed at high emission angles in less than 1/3 of the ALMA observations and includes an equatorial area (longitude $\sim 90^\circ\text{W}$, latitudes $\pm 30^\circ$) where unmapped topography could be present (Shepard et al., 2021). We remove from the maps those areas that have a bad goodness of fit, that is, $\chi_r^2 > 10$ (the optimal value is $\chi_r^2 \sim 1$), or $N_{obs} \leq 3$. The latter condition follows from Equations 4 and 5, where a surface area shall be visible a number of times at most equal to the number of degrees of freedom plus one in order for the inverse problem to be well-conditioned. At least two data points are needed to derive the best-fit value of Γ (which controls the variation of temperature as a function of time), and another data point is needed to break the degeneracy on the best-fit value of ϵ . However, if a surface area is observed just for a few epochs near the terminator and then it rotates away from sight, its surface properties may remain unconstrained even if $N_{obs} \geq 3$. To assess the minimum required number of N_{obs} to fit the data, we test the fitting procedure in Section 2.4 to retrieve the surface properties of synthetic Psyche's images with added Gaussian noise based on σ_D from the data. We confirm that constraining a solution for $N_{obs} \geq 3$ is possible everywhere on Psyche despite for a few areas at the south pole, which we remove from the map.

3. Results

3.1. Comparison Between the Global Solution and the Local Solution

Figure 2a is the map of brightness temperature corresponding to the time-averaged thermal emission observed with ALMA, that is, the brightness temperature corresponding to the observed thermal emission averaged across the different epochs when the location was visible. Figures 2b and 2c are maps of the time-averaged model brightness temperature and time-averaged residual brightness temperature, respectively, for a smooth surface with $\Gamma = 283$ tiu and $\epsilon = 18.5$ which is the global best-fit case from de Kleer, Cambioni, and Shepard (2021). Figures 2d and 2e are the maps of the time-averaged model brightness temperature and time-averaged residual brightness temperature obtained by fitting a value of Γ and ϵ to the thermal emission curve of each area on Psyche (this study). Hereafter, we will refer to the results in panels (b) and (c) as the “global solution” and those in panels (d) and (e) as the “local solution.” We find that the structures in the temperature residual map of the global solution (Figure 2c) are well explained by a variegation in thermal inertia and dielectric constant over the surface: the residuals for the local solution (Figure 2e) are randomly distributed over the surface with mean value and standard deviation equal to -0.3 and 1.3 K, respectively.

3.2. Maps of Thermal Inertia and Dielectric Constant

Figure 3 displays the maps of Psyche's surface properties derived from the ALMA data: thermal inertia Γ (best-fit value: panel a; uncertainty: panel b); dielectric constant ϵ (best-fit value: panel c; uncertainty: panel d); the goodness-of-fit of the local solution (panel e); and the surface coverage achieved with ALMA (panel f), that is, how many times a surface area was observed by ALMA. The areal abundance of surface areas with a certain value of thermal inertia, dielectric constant and goodness-of-fit is displayed in Figure 4, together with the corresponding cumulative distributions (red curves). Most areas have $\chi^2_r < 5-6$, which we consider satisfactory for these types of observations.

We find that the surface thermal inertia of Psyche ranges between ~ 25 tiu and ~ 600 tiu, although most of the surface has a thermal inertia in the range $150-300$ tiu (Figures 3a and 4a). To the west of longitude 30°W , we observe that the uncertainty of the thermal inertia measurements (Figure 3b) are comparable to the best-fit values of the thermal inertia, that is, the measurements are not well constrained, while the thermal inertia measurements are better constrained in most of the Eastern hemisphere. This is probably because the Western hemisphere was observed a fewer number of epochs (and hence times of day) than the Eastern hemisphere (Figure 3f). In areas with thermal inertia $\Gamma > 300$ tiu, the best-fit thermal inertia tend to have higher uncertainties because the diurnal curves of the thermal emission become more and more alike as the surface thermal inertia increases.

We find that the dielectric constant of Psyche's surface material ranges between ~ 8 and ~ 60 (Figures 3c and 4b), although most of the surface has dielectric constant in the range $15-25$, consistent with the global solution by de Kleer, Cambioni, and Shepard (2021). Analogously to the thermal inertia measurements, the highest uncertainties for the dielectric constant are observed in the Western hemisphere likely because of lower surface coverage (Figure 3f). Overall, the measured dielectric constant values have much lower uncertainties than the thermal inertia values.

3.3. Thermal Signature of a Large Mass-Deficit Region

In the Eastern hemisphere (where the values of thermal inertia are better constrained), we observe a prominent feature in the thermal inertia map extending between longitudes 15°W and 60°E (i.e., the region in the dashed white box in Figures 3a and 5a). The feature is a low-thermal-inertia region surrounded by a ring of high-thermal inertia areas and corresponds to the Bravo and Golf regions in Shepard et al. (2021). We refer to this region as “Bravo-Golf” hereafter. In Figure 5a, we plot the altitude map of Psyche computed by subtracting Psyche's best-fit ellipsoid to its shape model. Figure 5b is the same map of thermal inertia of Figure 3a with the altitude contours superimposed onto it. In Figure 5c, we plot both a thermal-inertia profile and an altitude profile (black and red curves, respectively) taken along longitude 35°E . We observe that the two profiles closely resemble one another, and that the thermal inertia of the lowlands is statistically distinct from that of the highlands.

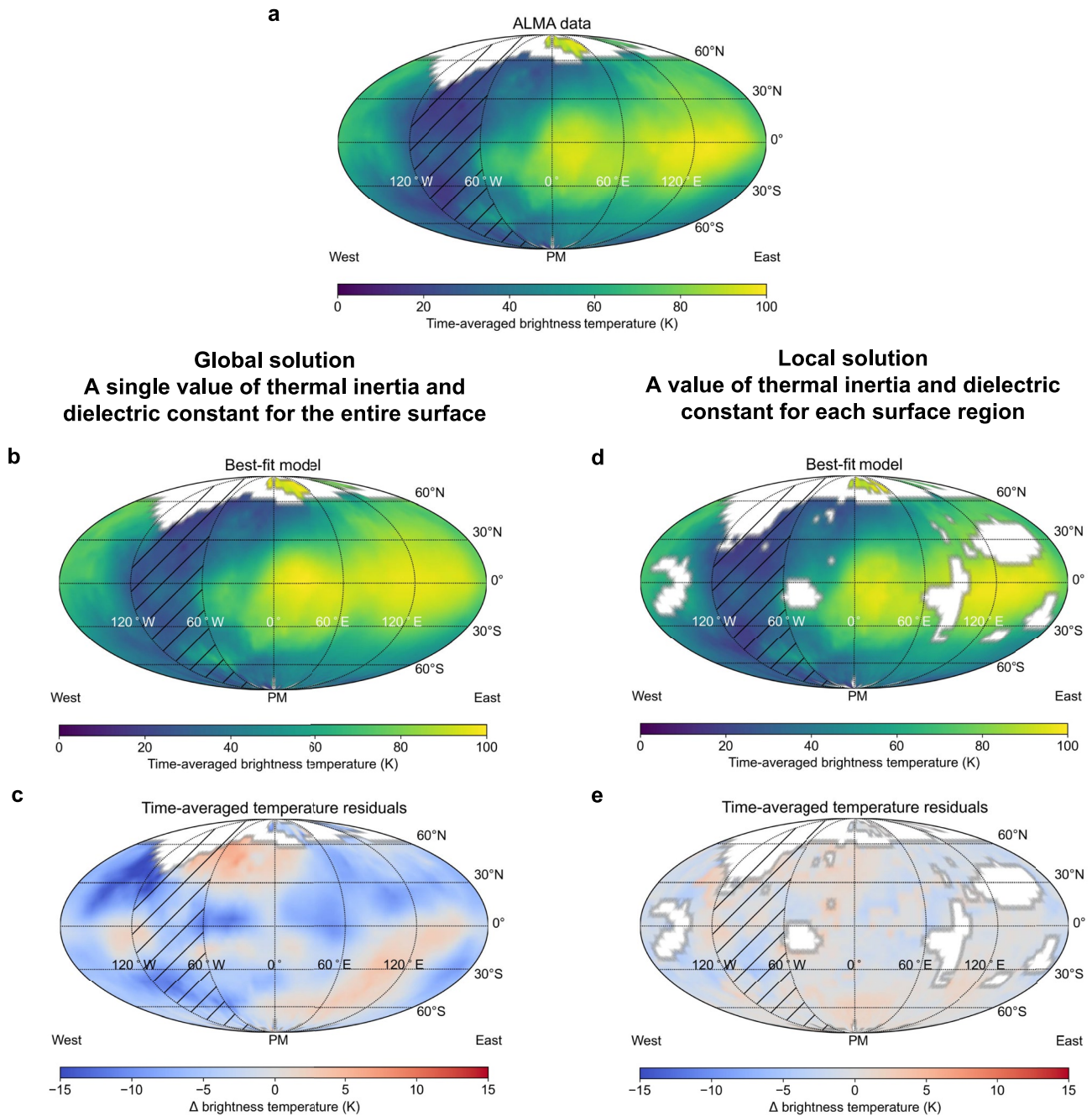


Figure 2. Atacama Large Millimeter Array (ALMA) data (top panel), global solution (left panels) and local solution (right panels) of the thermal emission of Psyche. (a), Time-averaged brightness temperature corresponding to the ALMA data. (b), Time-averaged brightness temperature corresponding to the best-fit surface properties in de Kleer, Cambioni, and Shepard (2021). (c), Time-averaged residual brightness temperature (i.e., time-average of the model minus the data) for the model in panel (b). (d), Time-averaged brightness temperature corresponding to the best-fit properties for each surface area (this study). (e), Time-averaged residual brightness temperature for the model in panel (d). In panels (d) and (e), we removed the areas that were either observed less than 3 times or have bad goodness of fit ($\chi^2_r > 10$). The hatched region is where possible model artifacts may affect the quality of the solution (see Section 2.5). The meridians are spaced 60° apart, so that “West” indicates PM − 180° and “East” indicates PM + 180°. The parallels are spaced 30° apart. The sub-observer point is at latitude −14°, around which the resolution of the maps is estimated to be ~5°.

To take into account the uncertainties in the value of thermal inertia, we perform a two-sided Spearman test to try the null hypothesis that a random distribution in thermal inertia and elevation in-between longitudes 15°W and 60°E and latitudes ±50° could reproduce the observed feature. We perform the test 10,000 times, where at each trial we draw sample from a Gaussian distribution with mean and standard deviation equal to the best-fit Γ

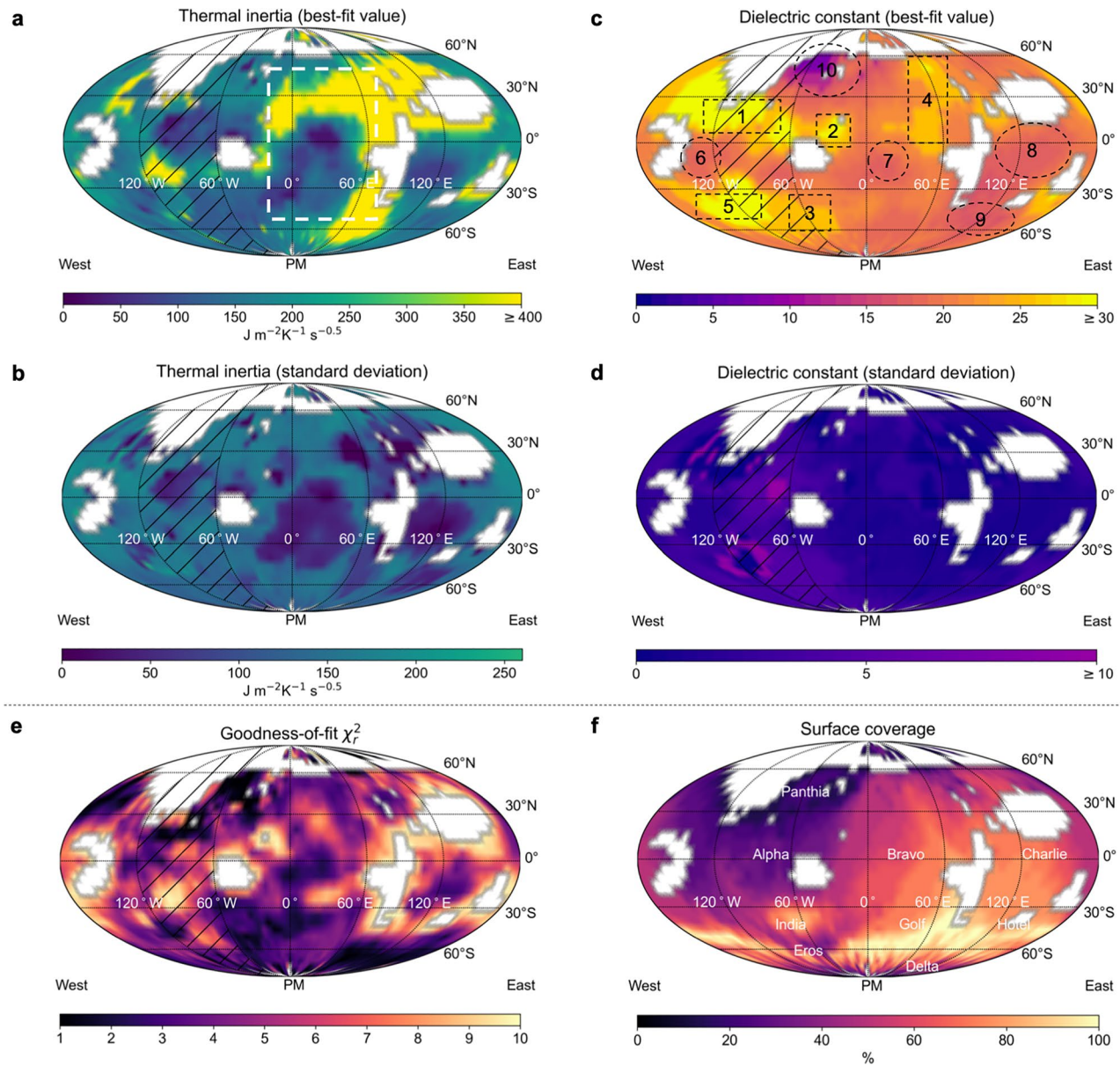


Figure 3. Maps of thermal inertia and dielectric constant of asteroid (16) Psyche derived from the Atacama Large Millimeter Array (ALMA) thermal emission data. (a) Best-fit thermal inertia. (b) Uncertainty of the thermal inertia. (c) Best-fit dielectric constant. (d) Uncertainty of the dielectric constant. (e) Goodness-of-fit in units of χ^2_r (Equation 4). (f) Surface coverage (i.e., how many times a surface area was observed by ALMA). In panel (a), the dashed box indicates the Bravo-Golf region discussed in Sections 3.3 and 4.2. In panel (c) we indicate 10 areas whose surface material has median dielectric constant at least 1 standard deviation higher (squares, labeled 1–5) or lower (circles, labeled 6–10) than the median global value of Psyche. For the significance of these comparisons and their interpretation, see Section 4.1. The names of surface area in panel (f) are from Shepard et al. (2021). 3-D animations of panels (a and c) are available as supporting information (videos S1 and S2 in Supporting Information S1, respectively).

and its uncertainty. We find that the correlation between altitude and thermal inertia in the region is statistically significant as the null hypothesis has a probability below 10^{-5} in each trial (Figure 5d). We discuss the thermal-inertia feature in Section 4.2.

3.4. Robustness of the Results Against Model Assumptions

We test the robustness of the results to the assumed value of Bond albedo (Section 2.3). Variations in albedo on Psyche were observed by Viikinkoski et al. (2018), who assumed that the albedo could vary up to $\pm 25\%$ of the nominal value—a reasonable range given that the problem of extracting albedo variations from lightcurves is

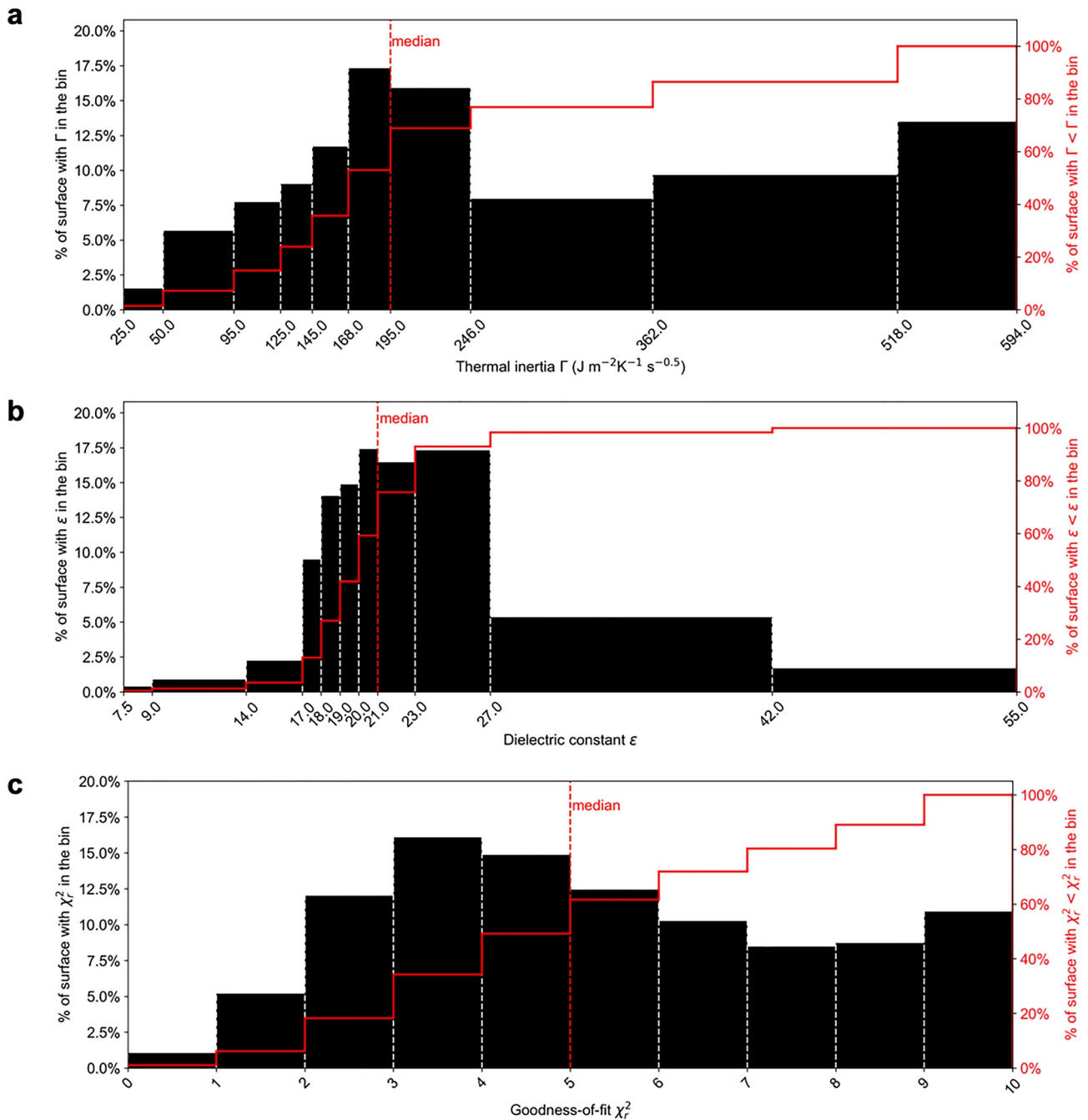


Figure 4. Most of Psyche's surface has thermal inertia $\sim 150\text{--}300 \text{ J m}^{-2} \text{K}^{-1} \text{s}^{-0.5}$ and dielectric constant $\sim 15\text{--}25$, consistent with the global values presented by de Kleer, Cambioni, and Shepard (2021). (a), Thermal inertia. (b), Dielectric constant. (c), Goodness-of-fit. The black histograms display abundance of surface areas with Γ , ϵ or χ^2_r in the bin. The values are those from the maps of Figure 3, weighted according to the corresponding area on the best-fit ellipsoid by Shepard et al. (2021). The red curves are the corresponding cumulative distributions. For panels (a) and (b), the bin edges correspond to the midpoints between consecutive values of Γ and ϵ explored with the thermophysical model (Section 2).

poorly constrained. Using instantaneous thermal equilibrium, de Kleer, Cambioni, and Shepard (2021) demonstrated that a variation of $\pm 30\%$ in Bond albedo is too small to explain the magnitude of the time-averaged temperature residuals in Figure 2c. We confirm this by running additional TPM simulations for the global model of de Kleer, Cambioni, and Shepard (2021), but with 30% higher/lower albedo than the nominal case. While we cannot exclude that the thermal anomalies are in part contributed by differences in temperature driven by albedo

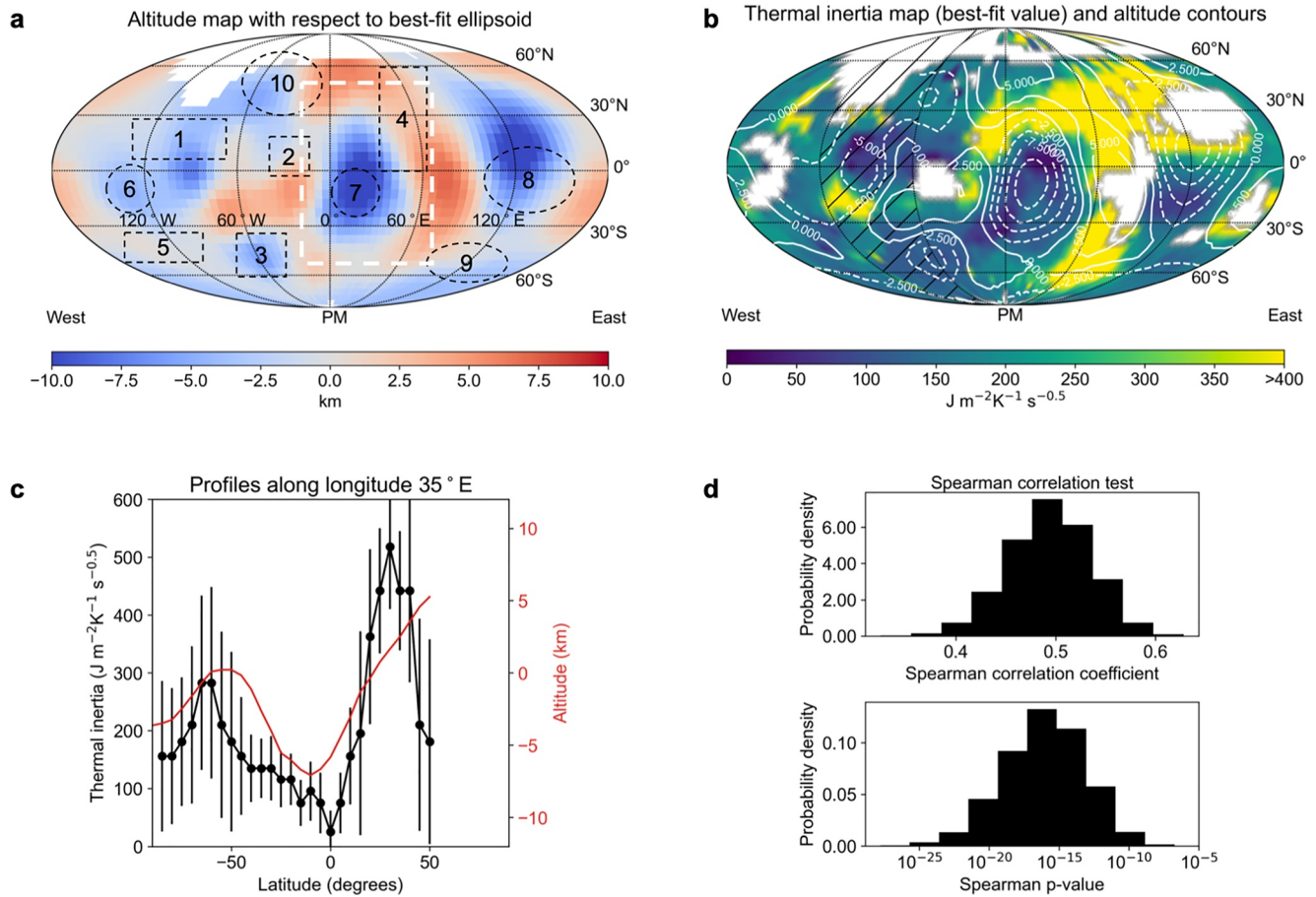


Figure 5. The lowlands in the Bravo-Golf region (longitudes 15°W to 60°E) have a lower thermal inertia than the surrounding highlands. (a), Altitude map computed by subtracting the best-fit ellipsoid of Psyche from its shape model by Shepard et al. (2021). The dashed white box indicates the Bravo-Golf region analyzed in Section 3.3 and discussed in Section 4.2. We also indicate the same 10 areas of Figure 3c whose surface material has median dielectric constant at least 1 standard deviation higher (squares, labeled 1–5) or lower (circles, labeled 6–10) than the median global value of Psyche (Section 4.1). (b), Altitude contours superimposed on the map of best-fit thermal inertia of Figure 3a. (c), Latitudinal profiles at longitude 35°E of thermal inertia and altitude (black and red curves, respectively). (d), Results of the two-sided Spearman test of the null hypothesis that a random distribution of thermal-inertia- and elevation-values could produce the observed correlation of panel (b) when uncertainties in thermal inertia are considered, for values in-between longitudes 15°W and 60°E and latitudes $\pm 50^\circ$. The Spearman p-value is lower than 10^{-5} in all the 10,000 trials, which confirms that thermal inertia directly correlates with altitude in the region.

variations, we conclude that the anomalies are mainly due to heterogeneity in the thermal inertia and dielectric constant of the surface materials.

Next, we test the robustness of the results to the assumption of smooth surface (i.e., $f = 0^\circ$, Section 2.3). We run additional simulations in which we carve on each facet an hemispherical crater with area equal to 60% of that of the facets (“rough model”). This corresponds to a root-mean-square slope of $f \sim 40^\circ$ whose effect on emissivity is modeled as done in de Kleer, Cambioni, and Shepard (2021). We experiment with $\Gamma = (116, 283, 442)$ tiu, which correspond to the lower quartile in Figure 4a, the best-fit global value from de Kleer, Cambioni, and Shepard (2021), and the upper quartile in Figure 4a, respectively. Figure 6 is a map of those areas on Psyche where the rough model has a better goodness of fit than the smooth model, that is, $\chi_r^2(\text{rough}) < \chi_r^2(\text{smooth})$ (Equation 4). We find that $\chi_r^2(\text{rough}) > 10$ for most of the surface and that, in the few areas where $\chi_r^2(\text{rough}) < \chi_r^2(\text{smooth})$, the difference between $\Gamma(\text{rough})$ and $\Gamma(\text{smooth})$ is within the uncertainty of $\Gamma(\text{smooth})$. The thermal-inertia solution in the Bravo-Golf region has $\chi_r^2(\text{smooth}) < \chi_r^2(\text{rough})$ in most of the lowlands and $\chi_r^2(\text{rough}) > 10$ in the highlands, suggesting that the thermal-inertia signature analyzed in Section 3.3 is unlikely to be due to unmodelled roughness. We conclude that a smooth surface is a good assumption not only globally, but also locally.

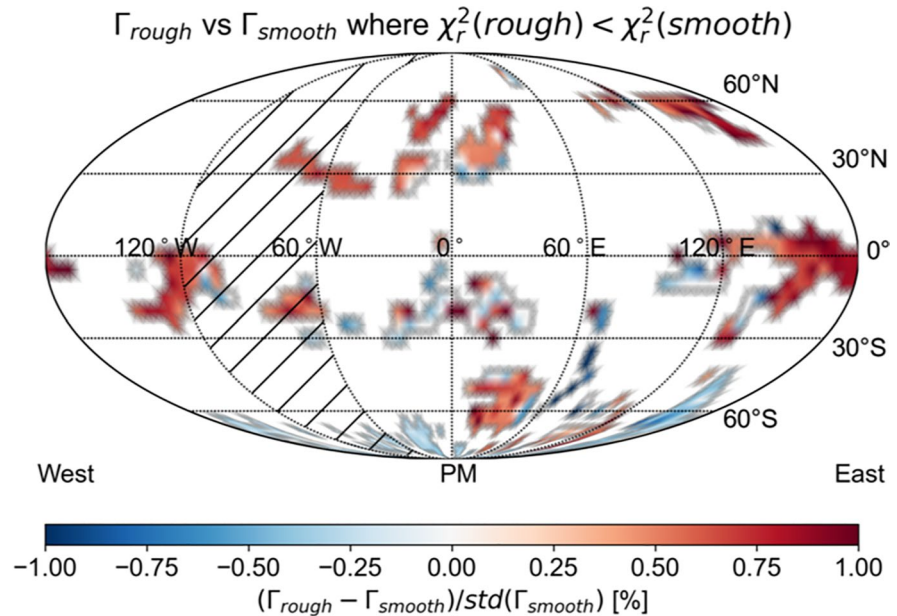


Figure 6. Tests of robustness of the results. Relative difference between the thermal inertia $\Gamma(\text{rough})$ obtained using the rough model and thermal inertia $\Gamma(\text{smooth})$ obtained using the smooth model, normalized to the standard deviation of the latter. The map plots those (few) areas where the rough solution has better goodness of fit than the smooth solution (i.e., $\chi_r^2(\text{rough}) < \chi_r^2(\text{smooth}) < 10$).

4. Discussion and Interpretation of the Results

In Section 4.1, we interpret the variations of Psyche's dielectric constant in terms of metal content of the uppermost few millimeters of regolith. In Section 4.2, we discuss the thermal signature of the Bravo-Golf region (i.e., the region delimited by the dashed white box in Figures 3a and 5a) and propose three scenarios that may explain it.

4.1. Relative Abundance of Metals and Silicates Over the Surface

The thermal inertia values of most of Psyche's surface ($\Gamma \sim 150\text{--}300$ tui) is consistent with a metal-rich surface as previously noted by Matter et al. (2013) and de Kleer, Cambioni, and Shepard (2021). Our results are also consistent with the low-emissivity case from Landsman et al. (2018), who measured a thermal inertia of 100–200 tui for an emissivity of 0.5 and 0.7, although their high-emissivity case finds a lower thermal inertia of 5–25 tui. The dielectric constant of most of Psyche's surface ($\epsilon \sim 15\text{--}25$) is also consistent with a metal-rich surface because it is higher than the typical range of Earth rocks ($\epsilon \sim 2\text{--}10$) and closer to that of meteorites with high metal content (e.g., Campbell & Ulrichs, 1969).

Intriguingly, we do not observe a global correlation between thermal inertia and dielectric constant on Psyche. Interpreting this finding requires new laboratory measurements of thermal conductivity of metal-rich particulates and their dielectric constants at ALMA-relevant frequencies. Numerous laboratory measurements of the dielectric constant of terrestrial rocks and meteorites exist in the range 20 MHz–35 GHz (Campbell & Ulrichs, 1969; Hickson et al., 2020; Parkhomenko, 1967). By contrast, laboratory data for rocks at millimeter wavelengths ($\sim 100\text{--}300$ GHz) are very limited (e.g., Brouet et al., 2014), and there are not data for powdered metals.

While most of Psyche's surface has dielectric constant in-between 15–25, we also observe areas whose dielectric constant ranges between ~ 8 to ~ 60 . Assuming that the metal on Psyche is in the form of metallic inclusions (de Kleer, Cambioni, & Shepard, 2021), $\epsilon = 60$ corresponds to porosity lower than 25% and a metal content $> 40\%$, while the porosity and metal content are unconstrained for $\epsilon \sim 5$. These calculations assume no reduction in emissivity due to volume scattering (see figure 8c in de Kleer, Cambioni, and Shepard (2021)). As such, the dielectric constant measurements (Figure 3c) suggest that the relative abundance of metals and silicates of the first millimeters of regolith varies across the surface.

We observe that the regions labeled as n. 1, 2, 3, 4 and 5 in Figures 3c and 5a and centered at $\sim(15^\circ\text{N}, 100^\circ\text{W})$, $(10^\circ\text{N}, 15^\circ\text{W})$, $(45^\circ\text{S}, 60^\circ\text{W})$, $(30^\circ\text{N}, 60^\circ\text{E})$, and $(40^\circ\text{S}, 120^\circ\text{W})$ have dielectric constant ~ 4.9 , 2.6 , 2.6 , 1.0 , and 4.9 standard deviations higher than the median dielectric constant of Psyche, respectively. This is indicative of a locally higher metal content of the first millimeters of the surface. Intriguingly, areas n. 1, 2, and 3 are in proximity of large depressions of Psyche's shape (Figures 5a and Shepard et al., 2021) where ferrovolcanism, that is, eruption of metallic lava flows on the surface, could have preferentially occurred (Abrahams & Nimmo, 2019; Johnson et al., 2020). Abrahams and Nimmo (2019) showed that molten iron may erupt on the surface of a pure iron-nickel remnant. If there is a silicate layer on top of the core, the iron melt may create intrusive diapirs which can be successively uncovered through excavation by impacts (Raducan et al., 2020). Johnson et al. (2020) showed that, if Psyche is a differentiated object with a relatively thin silicate mantle and iron core, volatile-rich molten iron could be injected into the mantle and erupt on the surface during its cooling. They do not provide specific predictions on the eruption sites, but suggest that these are more favored where the crust/mantle are the thinnest, which could be associated with large depressions.

The areas labeled as n. 6, 7, 8, 9 and 10 in Figures 3c and 5 and centered at $\sim(10^\circ\text{S}, 130^\circ\text{W})$, $(15^\circ\text{S}, 15^\circ\text{E})$, $(5^\circ\text{S}, 130^\circ\text{E})$, $(50^\circ\text{S}, 120^\circ\text{E})$, and $(50^\circ\text{N}, 50^\circ\text{W})$ have dielectric constant ~ 1 , 1 , 1.5 , 1.5 , and 4.4 standard deviations lower than the median dielectric constant of Psyche, respectively. This is indicative of a locally lower metal content of the first millimeters of the surface. The surface materials at these locations could be a mixture between metal- and silicate-rich materials. The presence of silicate materials on Psyche in the form of orthopyroxenes was proposed by Sanchez et al. (2017) to explain the detection of the $0.93\text{-}\mu\text{m}$ band in the visible near-infrared spectra of Psyche. Additionally, Hardersen et al. (2005), Fornasier et al. (2010) and Takir et al. (2017) detected the presence of the $3\text{-}\mu\text{m}$ band at longer wavelengths, which they associated with OH- or H_2O -bearing phases, possibly in the form of phyllosilicates (Takir & Emery, 2012). The carbonaceous materials are likely exogenic (e.g., Avdellidou et al., 2018; Shepard et al., 2015), consistent with experiments showing that hydrated projectiles may implant the $3\text{-}\mu\text{m}$ band on metal-rich surfaces (Libourel et al., 2019). Exogeneous silicates are therefore a likely contributor to the observed areas with low dielectric constant, but we cannot conclude that they are all predominantly carbonaceous, because dielectric constant is a poor discriminator of composition between different silicate-rich materials (Brecher et al., 1975; Palmer et al., 2015). Area n. 10 has the lowest dielectric constant on Psyche ($\epsilon \sim 8$) and could be particularly rich in silicate materials within the first millimeters of the surface. However, we caution that model artifacts could be present at that location because the region was imaged in less than $1/3$ of the ALMA observations and always at high emission angles.

Assuming that Psyche's surface material is a mixture of rocks and iron sulfides/oxides (equation 15 in de Kleer, Cambioni, & Shepard, 2021), the range of dielectric constant on Psyche corresponds to a local bulk density ranging from $\rho \sim 1500\text{ kg/m}^3$ (i.e., 100 wt.% iron sulfides/oxides and 67% macroporosity) to 4500 kg/m^3 (i.e., 97 wt.% iron sulfides/oxides and 0% macroporosity). This density range encompasses the radar-derived $\rho = 3500\text{ kg/m}^3$ (which we assumed for Equation 1) and may also be consistent with the full density range inferred from the full range of measured radar albedos by Shepard et al. (2021). However, we do not observe a spatial correlation between dielectric constant and radar albedo on Psyche. For example, area n. 3 (India in Shepard et al., 2021) is a region of both high dielectric constant and elevated radar albedo, but area n. 9 (Hotel in Shepard et al., 2021) is a radar-bright area with low dielectric constant. Radar-bright regions with low ALMA dielectric constant could be metal-rich areas covered by a thin mantle of silicate-rich material or be covered in a silicate-rich regolith with embedded metal particles. We cannot disentangle these two scenarios just based on dielectric constant and thermal inertia alone because our model assumes constant density with depth. In fact, the density of the uppermost millimeters of the surface (to which ALMA is sensitive to) can be different than that of the underlying first tens of centimeters, to which the radar is sensitive to. The latter is certainly true for the Moon (Hayne et al., 2017). Further research is therefore warranted to adjust radar densities to observations at ALMA wavelengths. This task offers many challenges, including limitations of current techniques to convert radar albedo and dielectric constant into bulk density of the regolith, the different spatial resolutions of radar versus ALMA measurements, and the lack of measurements of the dielectric properties of metal-rich materials in both solid and particulate form at ALMA wavelengths.

4.2. Thermal Inertia of the Bravo-Golf Region

Here we propose three non-mutually-exclusive scenarios to explain why the thermal inertia of the lowlands of the Bravo-Golf region is systematically lower than that of the highlands. The three scenarios are sketched in Figure 7.

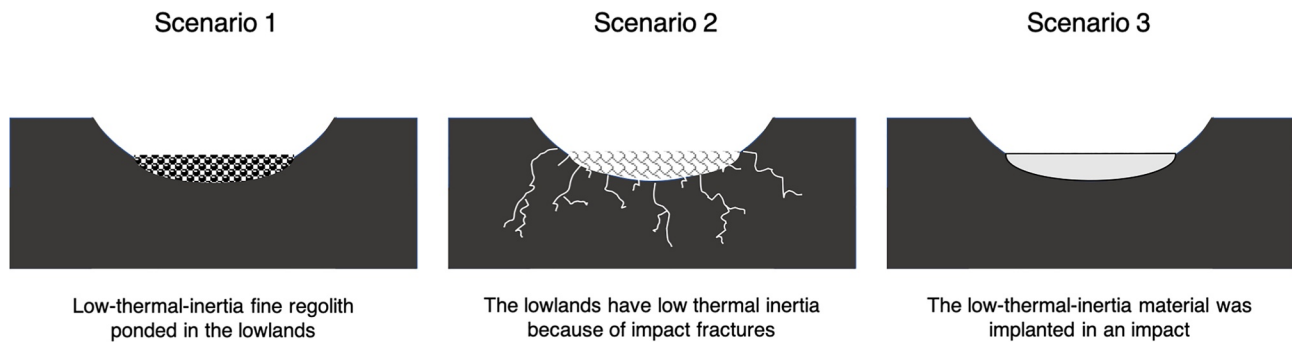


Figure 7. The three possible scenarios proposed to explain the thermal-inertia contrast between the lowlands and the highlands in the Bravo-Golf region. The scenarios are described in Section 4.2.

A first hypothesis is that the lowlands are metal-rich (thus radar-bright as observed by Shepard et al., 2021), but covered in a thin mantle of fine regolith, which lowers their thermal inertia with respect to the highlands where the regolith has coarser particle size. For a regolith particulate, thermal conductivity increases with increasing particle size for a given bulk density and specific heat capacity (e.g., Cambioni et al., 2019; Sakatani et al., 2018). On airless worlds, impacts may induce accumulation of low-thermal-inertia fine regolith in places where the gravity field is the highest. The Bravo-Golf region could be a place where fine material preferentially ponds because it is closer to the center of mass of Psyche than any other point on the surface. A similar argument was presented for the bi-lobate asteroid (216) Kleopatra by Shepard et al. (2018) who, based on the analysis of asteroid geopotential surface, suggested that loose material should preferentially migrate to Kleopatra's neck region, consistent with radar observations. On Psyche, we speculate that the large impacts which formed some of its depressions may have kicked-up fine regolith and/or generated seismic shaking which provoked accumulation of fines in the lowlands of the Bravo-Golf region. On asteroids greater than 100 km in diameter, individual impacts are expected to induce only localized (regional) seismic effects, but large impacts may still have widespread effects on the surface (Richardson et al., 2005).

A second hypothesis is that the surface material covering the lowlands is more porous than that of the highlands. Rock's thermal inertia decreases with increasing rock porosity (e.g., Cambioni et al., 2021; Grott et al., 2019), although measurements of meteorite thermal conductivity as function of porosity are primarily based on chondrites. Rock porosity can be enhanced by impact-induced fractures. Laboratory experiments of hypervelocity impacts onto iron-nickel meteorite and ingots (Libourel et al., 2019; Marchi et al., 2020; Matsui & Schultz, 1984) show that the fractures permeate the floor of the crater, while the rims acquire a rose-petal-shaped configuration and are not fractured, although results could be affected by edge effects in the samples. If the fractures extend to the entire body, this may potentially explain the low density of some M-type asteroids (e.g., Psyche and Kleopatra, Elkins-Tanton et al., 2020; Marchis et al., 2021). Alternatively, the surface could be covered in highly porous boulders, whose thermal inertia could mimic that of fine regolith (Cambioni et al., 2021; Grott et al., 2019; Okada et al., 2020; Rozitis et al., 2020). This scenario, however, is unlikely for Psyche if its surface material has a composition analogous to that of iron meteorites (porosity <10%, Macke, 2010) or mesosiderites (porosity ~12%, similar to the ~14% of LL chondrites, but much lower than ~30% of CM chondrites, Britt & Consolmagno, 2003).

A third hypothesis is that the lowlands have a higher abundance of silicate-rich materials than the highlands, consistent with having lower dielectric constant than some areas of the highlands (e.g., area 7 vs. area 4 in Figure 3c). The silicate-rich materials could be the residue of a silicate impactor that may have formed the Bravo-Golf depression and whose material was mixed with the (metal-rich, thus radar-bright, Shepard et al., 2021) subsurface material by subsequent smaller impacts. If that is the case, we speculate that Psyche's surface was behaving in a ductile way at the time of impact that formed the Bravo-Golf depression, because projectile implantation efficiency is close to zero for most cooled impacts (Marchi et al., 2020), assuming a target composition as that of iron meteorites. We nevertheless caution that impact contamination is unlikely to be limited to the crater floor (Libourel et al., 2019; Marchi et al., 2020) and the highlands have lower albedo than the lowlands (Viikinkoski et al., 2018), in contrast with the findings by Libourel et al. (2019) that silicate implantation lowers the albedo of the crater with respect to exposed iron.

5. Conclusion

We present a new analysis of the ALMA thermal emission data of asteroid (16) Psyche published in de Kleer, Cambioni, and Shepard (2021) using a model which derives a value of thermal inertia and dielectric constant for each region on the surface. We find that most of Psyche's surface has thermal inertia in-between 150–300 tiu and dielectric constant in-between 15–25.

Our results support the metal-rich nature of Psyche's surface materials, consistent with previous studies (Matter et al., 2013). Because our data spatially resolve the surface, we also observe heterogeneity in the surface properties due to the presence of terrains whose thermal inertia range between ~25 tiu and ~600 tiu and dielectric constant between ~8 and ~60. However, we do not observe a direct correlation between thermal inertia and dielectric constant on Psyche's surface. The array of detected dielectric constant values is indicative of a mineralogy of the first millimeters of the surface ranging from low-metal to high-metal content depending on porosity. Some metal-rich areas with high dielectric constant correspond to depressions where ferrovolcanism (Abrahams & Nimmo, 2019; Johnson et al., 2020) could have preferentially occurred. Other regions with low dielectric constant could have higher abundance of silicate materials mixed with metals. This is consistent with spectroscopic evidence of orthopyroxenes on Psyche (Sanchez et al., 2017) and hydrated minerals (Takir et al., 2017) of likely exogeneous origin (Avdellidou et al., 2018). In the thermal inertia map, we observe that the lowlands of a large depression (dubbed Bravo-Golf and located between longitudes 15°W and 60°E) have statistically lower thermal inertia than the surrounding highlands. We propose that this could be a signature of a thin mantle of fine regolith covering the lowlands; presence of fractures induced by impacts; and/or silicate materials implanted by impacts. All three scenarios are indicative of a collisionally evolved surface.

In conclusion, we provide evidence that Psyche is a metal-rich asteroid whose surface is heterogeneous, shows both metal and silicate materials, and appear evolved by impacts. We look forward to the data from the NASA Psyche mission to get new insight into this unusual and fascinating world.

Conflict of Interest

The authors declare no conflicts of interest relevant to this study.

Data Availability Statement

The ALMA data are freely available at the ALMA data archive (<https://almascience.nrao.edu/alma-data>) under the project code: 2018.1.01271.S. The paper makes use of the ThermoPhysical Model by Delbo et al. (2015), which is publicly available at <https://www.oca.eu/en/marco-delbo> in the section “Asteroid thermal models”, and the software package PyVista by Sullivan and Kaszynski (2019). All the relevant equations and parameters for the reproducibility of the results are given in this paper and in de Kleer, Cambioni, and Shepard (2021). Datasets for this research are available in these in-text data citation references: results in Cambioni et al. (2022); shape model in Shepard et al. (2021) (direct link in caption of their Figure 7).

References

- Abrahams, J. N. H., & Nimmo, F. (2019). Ferrovolcanism: Iron volcanism on metallic asteroids. *Geophysical Research Letters*, 46(10), 5055–5064. <https://doi.org/10.1029/2019GL082542>
- Ali-Lagoa, V., Müller, T. G., Usui, F., & Hasegawa, S. (2018). The AKARI IRC asteroid flux catalogue: Updated diameters and albedos. *Astronomy and Astrophysics*, 612, A85. <https://doi.org/10.1051/0004-6361/201731806>
- Altenhoff, W. J., Johnston, K. J., Stumpff, P., & Webster, W. J. (1994). Millimeter-wavelength observations of minor planets. *Astronomy and Astrophysics*, 287, 641–646. <https://ui.adsabs.harvard.edu/abs/1994A&A...287..641A>
- Asphaug, E., & Reufer, A. (2014). Mercury and other iron-rich planetary bodies as relics of inefficient accretion. *Nature Geoscience*, 7(8), 564–568. <https://doi.org/10.1038/ngeo2189>
- Avdellidou, C., Delbo, M., & Fienga, A. (2018). Exogenous origin of hydration on asteroid (16) Psyche: The role of hydrated asteroid families. *Monthly Notices of the Royal Astronomical Society*, 475(3), 3419–3428. <https://doi.org/10.1093/mnras/sty017>
- Bell, J. F., Davis, D. R., Hartmann, W. K., & Gaffey, M. J. (1989). Asteroids: The big picture. In R. P. Binzel, T. Gehrels, & M. S. Matthews (Eds.), *Asteroids II* (pp. 921–945).
- Birlan, M., Vernazza, P., & Nedelcu, D. A. (2007). Spectral properties of nine M-type asteroids. *Astronomy and Astrophysics*, 475(2), 747–754. <https://doi.org/10.1051/0004-6361:20077914>
- Brecher, A., Briggs, P. L., & Simmons, G. (1975). The low-temperature electrical properties of carbonaceous meteorites. *Earth and Planetary Science Letters*, 28(1), 37–45. [https://doi.org/10.1016/0012-821X\(75\)90071-0](https://doi.org/10.1016/0012-821X(75)90071-0)

Acknowledgments

This paper makes use of the following ALMA data: ADS/JAO.ALMA#2018.1.01271.S. ALMA is a partnership of ESO (representing its member states), NSF (USA) and NINS (Japan), together with NRC (Canada), MOST and ASIAA (Taiwan), and KASI (Republic of Korea), in cooperation with the Republic of Chile. The Joint ALMA Observatory is operated by ESO, AUI/NRAO and NAOJ. The National Radio Astronomy Observatory is a facility of the National Science Foundation operated under cooperative agreement by Associated Universities, Inc. This research was funded in part by the Heising-Simons Foundation through grant 2019-1611. S. Cambioni acknowledges funding through the Crosby Postdoctoral fellowship of the Department of Earth, Atmospheric and Planetary Sciences, Massachusetts Institute of Technology. The authors thank M. Delbo and B. Weiss for insightful discussions and the reviewers for feedback that improved this manuscript.

- Britt, D. T., & Consolmagno, G. J. (2003). Stony meteorite porosities and densities: A review of the data through 2001. *Meteoritics & Planetary Sciences*, 38(8), 1161–1180. <https://doi.org/10.1111/j.1945-5100.2003.tb00305.x>
- Brouet, Y., Levasseur-Regourd, A. C., Encrenaz, P., & Gulkis, S. (2014). Permittivity of porous granular matter, in relation with Rosetta cometary mission. *Planetary and Space Science*, 103, 143–152. <https://doi.org/10.1016/j.pss.2014.08.012>
- Busarev, V. V. (2002). Hydrated silicates on M-, S- and E-type asteroids as possible traces of collisions with bodies from the Jupiter growth zone. *Solar System Research*, 36(1), 35–42. <https://doi.org/10.1023/a:1014221510387>
- Cambioni, S., de Kleer, K., & Shepard, M. (2022). Maps of thermal inertia, dielectric constant and brightness temperature of asteroid (16) Psyche derived from ALMA data. *Zenodo*. <https://doi.org/10.5281/zenodo.6321315>
- Cambioni, S., Delbo, M., Poggiali, G., Avdellidou, C., Ryan, A., Deshapriya, J., et al. (2021). Fine-regolith production on asteroids controlled by rock porosity. *Nature*, 598(7879), 49–52. <https://doi.org/10.1038/s41586-021-03816-5>
- Cambioni, S., Delbo, M., Ryan, A. J., Furfaro, R., & Asphaug, E. (2019). Constraining the thermal properties of planetary surfaces using machine learning: Application to airless bodies. *Icarus*, 325, 16–30. <https://doi.org/10.1016/j.icarus.2019.01.017>
- Campbell, M. J., & Ulrichs, J. (1969). Electrical properties of rocks and their significance for lunar radar observations. *Journal of Geophysical Research*, 74(25), 5867–5881. <https://doi.org/10.1029/JB074i025p05867>
- Chapman, C. R., & Salisbury, J. W. (1973). Comparisons of meteorite and asteroid spectral reflectivities. *Icarus*, 19(4), 507–522. [https://doi.org/10.1016/0019-1035\(73\)90078-X](https://doi.org/10.1016/0019-1035(73)90078-X)
- Clark, B. E., Bus, S. J., Rivkin, A. S., Shepard, M. K., & Shah, S. (2004). Spectroscopy of X-Type Asteroids. *The Astronomical Journal*, 128(6), 3070–3081. <https://doi.org/10.1086/424856>
- Clark, R. N. (2009). Detection of adsorbed water and hydroxyl on the Moon. *Science*, 326(5952), 562–564. <https://doi.org/10.1126/science.1178105>
- Consolmagno, G. J., & Britt, D. T. (2013). Iron meteorite density and heat capacity. *Meteoritics and Planetary Science Supplement*, 76, 5128.
- Consolmagno, G. J., Schaefer, M. W., Schaefer, B. E., Britt, D. T., Macke, R. J., Nolan, M. C., & Howell, E. S. (2013). The measurement of meteorite heat capacity at low temperatures using liquid nitrogen vaporization. *Planetary and Space Science*, 87, 146–156. <https://doi.org/10.1016/j.pss.2013.07.009>
- Coradini, A., Capaccioni, F., Erard, S., Arnold, G., De Sanctis, M. C., Filacchione, G., et al. (2011). The surface composition and temperature of asteroid 21 Lutetia as observed by Rosetta/VIRTIS. *Science*, 334(6055), 492–494. <https://doi.org/10.1126/science.1204062>
- Davis, D. R., Farinella, P., & Marzari, F. (1999). The missing Psyche family: Collisionally eroded or never formed? *Icarus*, 137(1), 140–151. <https://doi.org/10.1006/icar.1998.6037>
- de Kleer, K., Butler, B., Cordiner, M., de Pater, I., Gurwell, M., Lazio, J., et al. (2021). Mapping satellite surfaces and atmospheres with ground-based radio interferometry. *Bulletin of the American Astronomical Society*, 53(4), 252. <https://doi.org/10.3847/25c2cfb.5e44dbf2>
- de Kleer, K., Butler, B., de Pater, I., Gurwell, M. A., Moullet, A., Trumbo, S., & Spencer, J. (2021). Ganymede's surface properties from millimeter and infrared thermal emission. *The Planetary Science Journal*, 2(1), 5. <https://doi.org/10.3847/PSJ/abcbf4>
- de Kleer, K., Cambioni, S., & Shepard, M. (2021). The surface of (16) Psyche from thermal emission and polarization mapping. *The Planetary Science Journal*, 2(4), 149. <https://doi.org/10.3847/PSJ/ac01ec>
- Delbo, M., Mueller, M., Emery, J. P., Rozitis, B., & Capria, M. T. (2015). Asteroid thermophysical modeling. In *Asteroids IV* (pp. 107–128). https://doi.org/10.2458/azu_uapress_9780816532131-ch006
- Delbo, M., & Tanga, P. (2009). Thermal inertia of main belt asteroids smaller than 100 km from IRAS data. *Planetary and Space Science*, 57(2), 259–265. <https://doi.org/10.1016/j.pss.2008.06.015>
- Delbo, M., Walsh, K., Bolin, B., Avdellidou, C., & Morbidelli, A. (2017). Identification of a primordial asteroid family constrains the original planetesimal population. *Science*, 357(6355), 1026–1029. <https://doi.org/10.1126/science.aam6036>
- DellaGiustina, D. N., Kaplan, H. H., Simon, A. A., Bottke, W. F., Avdellidou, C., Delbo, M., et al. (2021). Exogenic basalt on asteroid (101955) Benu. *Nature Astronomy*, 5(1), 31–38. <https://doi.org/10.1038/s41550-020-1195-z>
- DeMeo, F. E., Binzel, R. P., Slivan, S. M., & Bus, S. J. (2009). An extension of the Bus asteroid taxonomy into the near-infrared. *Icarus*, 202(1), 160–180. <https://doi.org/10.1016/j.icarus.2009.02.005>
- Elkins-Tanton, L. T., Asphaug, E., Bell, J. F., Bercovici, H., Bills, B., Binzel, R., et al. (2020). Observations, meteorites, and models: A preflight assessment of the composition and formation of (16) Psyche. *Journal of Geophysical Research*, 125(3), e06296. <https://doi.org/10.1029/2019JE006296>
- Elkins-Tanton, L. T., Asphaug, E., Bell, J. F., Bierson, C. J., Bills, B. G., Bottke, W. F., et al. (2022). Distinguishing the origin of asteroid (16) Psyche. *Space Science Reviews*, 218(3), 17. <https://doi.org/10.1007/s11214-022-00880-9>
- Elkins-Tanton, L. T., & Weiss, B. P. (2017). *Planetesimals: Early Differentiation and Consequences for Planets* (Vol. 16). Cambridge University Press.
- Elkins-Tanton, L. T., Weiss, B. P., Asphaug, E., Bottke, W. F., Binzel, R., & Wenkert, D. D. (2013). Differentiation in planetesimals with Applications to asteroid (16) Psyche. In *Lunar and planetary science conference*. (p. 1351). <https://ui.adsabs.harvard.edu/abs/2013LPI....44.1351E>
- Ferrais, M., Vernazza, P., Jorda, L., Rambaux, N., Hanuš, J., Carry, B., et al. (2020). Asteroid (16) Psyche's primordial shape: A possible Jacobi ellipsoid. *Astronomy and Astrophysics*, 638, L15. <https://doi.org/10.1051/0004-6361/202038100>
- Fornasier, S., Clark, B. E., & Dotto, E. (2011). Spectroscopic survey of X-type asteroids. *Icarus*, 214(1), 131–146. <https://doi.org/10.1016/j.icarus.2011.04.022>
- Fornasier, S., Clark, B. E., Dotto, E., Migliorini, A., Ockert-Bell, M., & Barucci, M. A. (2010). Spectroscopic survey of M-type asteroids. *Icarus*, 210(2), 655–673. <https://doi.org/10.1016/j.icarus.2010.07.001>
- Gouraud, H. (1971). Continuous shading of curved surfaces. *IEEE Transactions on Computers*, 100(6), 623–629. <https://doi.org/10.1109/t-c.1971.223313>
- Grott, M., Knollenberg, J., Hamm, M., Ogawa, K., Jaumann, R., Otto, K. A., et al. (2019). Low thermal conductivity boulder with high porosity identified on C-type asteroid (162173) Ryugu. *Nature Astronomy*, 3(11), 971–976. <https://doi.org/10.1038/s41550-019-0832-x>
- Gulkis, S., Keihm, S., Kamp, L., Backus, C., Janssen, M., Lee, S., et al. (2010). Millimeter and submillimeter measurements of asteroid (2867) Steins during the Rosetta fly-by. *Planetary and Space Science*, 58(9), 1077–1087. <https://doi.org/10.1016/j.pss.2010.02.008>
- Gulkis, S., Keihm, S., Kamp, L., Lee, S., Hartogh, P., Crovisier, J., et al. (2012). Continuum and spectroscopic observations of asteroid (21) Lutetia at millimeter and submillimeter wavelengths with the MIRO instrument on the Rosetta spacecraft. *Planetary and Space Science*, 66(1), 31–42. <https://doi.org/10.1016/j.pss.2011.12.004>
- Hanus, J., Delbo, M., Durech, J., & Ali-Lagoa, V. (2015). Thermophysical modeling of asteroids from WISE thermal infrared data—significance of the shape model and the pole orientation uncertainties. *Icarus*, 256, 101–116. <https://doi.org/10.1016/j.icarus.2015.04.014>
- Hardersen, P. S., Cloutis, E. A., Reddy, V., Mothé-Diniz, T., & Emery, J. P. (2011). The M-/X-asteroid menagerie: Results of an NIR spectral survey of 45 main-belt asteroids. *Meteoritics & Planetary Sciences*, 46(12), 1910–1938. <https://doi.org/10.1111/j.1945-5100.2011.01304.x>

- Hardersen, P. S., Gaffey, M. J., & Abell, P. A. (2005). Near-IR spectral evidence for the presence of iron-poor orthopyroxenes on the surfaces of six M-type asteroids. *Icarus*, 175(1), 141–158. <https://doi.org/10.1016/j.icarus.2004.10.017>
- Hardersen, P. S., Gaffey, M. J., Kumar, S., Fieber-Beyer, S. K., Crowell, J. J., & Crowell, A. M. (2007). Near-IR reflectance spectra of M-asteroids 250 Bettina, 369 Aeria, 413 Edburga, and 931 Whittemora. In *Lunar and planetary science conference*.
- Hayne, P. O., Bandfield, J. L., Siegler, M. A., Vasavada, A. R., Ghent, R. R., Williams, J.-P., et al. (2017). Global regolith thermophysical properties of the Moon from the Diviner Lunar Radiometer Experiment. *Journal of Geophysical Research: Planets*, 122(12), 2371–2400. <https://doi.org/10.1002/2017JE005387>
- Hickson, D. C., Boivin, A. L., Tsai, C. A., Daly, M. G., & Ghent, R. R. (2020). Modeling the dielectric properties of minerals from crystals to bulk powders for improved interpretation of asteroid radar observations. *Journal of Geophysical Research*, 125(7), e06141. <https://doi.org/10.1029/2019JE006141>
- Hunter, T. R., Hunter, T. R., Kneissl, R., Moullet, A., Brogan, C. L., Vlahakis, C., et al. (2015). The 2014 ALMA long baseline campaign: Observations of asteroid 3 Juno at 60 kilometer resolution. *The Astrophysical Journal Letters*, 808(1), L2. <https://doi.org/10.1088/2041-8205/808/1/L2>
- Johnson, B. C., Sori, M. M., & Evans, A. J. (2020). Ferrovolcanism on metal worlds and the origin of pallasites. *Nature Astronomy*, 4(1), 41–44. <https://doi.org/10.1038/s41550-019-0885-x>
- Keihm, S., Kamp, L., Gulkis, S., Hofstadter, M., Lee, S., Janssen, M., & Choukroun, M. (2013). Reconciling main belt asteroid spectral flux density measurements with a self-consistent thermophysical model. *Icarus*, 226(1), 1086–1102. <https://doi.org/10.1016/j.icarus.2013.07.005>
- Keihm, S. J. (1982). Effects of subsurface volume scattering on the lunar microwave brightness temperature spectrum. *Icarus*, 52(3), 570–584. [https://doi.org/10.1016/0019-1035\(82\)90017-3](https://doi.org/10.1016/0019-1035(82)90017-3)
- Lagerros, J. S. V. (1996). Thermal physics of asteroids. II. Polarization of the thermal microwave emission from asteroids. *Astronomy and Astrophysics*, 315, 625–632. <https://ui.adsabs.harvard.edu/abs/1996A&A...315..625L>
- Landsman, Z., Emery, J., Campins, H., Lim, L., & Cruikshank, D. (2019). Evidence for silicate regoliths on 27 main-belt M-type asteroids. *Thermops*, 1.
- Landsman, Z. A., Campins, H., Pinilla-Alonso, N., Hanuš, J., & Lorenzi, V. (2015). A new investigation of hydration in the M-type asteroids. *Icarus*, 252, 186–198. <https://doi.org/10.1016/j.icarus.2015.01.021>
- Landsman, Z. A., Emery, J. P., Campins, H., Hanuš, J., Lim, L. F., & Cruikshank, D. P. (2018). Asteroid (16) Psyche: Evidence for a silicate regolith from spitzer space telescope spectroscopy. *Icarus*, 304, 58–73. <https://doi.org/10.1016/j.icarus.2017.11.035>
- Lellouch, E., Moreno, R., Müller, T., Fornasier, S., Santos-Sanz, P., Moullet, A., et al. (2017). The thermal emission of Centaurs and trans-Neptunian objects at millimeter wavelengths from ALMA observations. *Astronomy and Astrophysics*, 608, A45. <https://doi.org/10.1051/0004-6361/201731676>
- Li, J.-Y., Moullet, A., Titus, T. N., Hsieh, H. H., & Sykes, M. V. (2020). Disk-integrated thermal properties of Ceres measured at millimeter wavelengths. *The Astronomical Journal*, 159(5), 215. <https://doi.org/10.3847/1538-3881/ab8305>
- Libourel, G., Nakamura, A. M., Beck, P., Potin, S., Ganino, C., Jacomet, S., et al. (2019). Hypervelocity impacts as a source of deceiving surface signatures on iron-rich asteroids. *Science Advances*, 5(8), eaav3971. <https://doi.org/10.1126/sciadv.aav3971>
- Macke, R. J. (2010). *Survey of meteorite physical properties density, porosity and magnetic susceptibility (Doctoral dissertation)*. University of Central Florida. Retrieved from <https://stars.library.ucf.edu/cgi/viewcontent.cgi?article=2637&context=etd>
- MacLennan, E. M., & Emery, J. P. (2021). Thermophysical investigation of asteroid surfaces. I. Characterization of thermal inertia. *The Planetary Science Journal*, 2(4), 161. <https://doi.org/10.3847/PSJ/ac1591>
- Magri, C., Nolan, M. C., Ostro, S. J., & Giorgini, J. D. (2007). A radar survey of main-belt asteroids: Arecibo observations of 55 objects during 1999–2003. *Icarus*, 186(1), 126–151. <https://doi.org/10.1016/j.icarus.2006.08.018>
- Marchi, S., Durda, D. D., Polanskey, C. A., Asphaug, E., Bottke, W. F., Elkins-Tanton, L. T., et al. (2020). Hypervelocity impact experiments in iron-nickel ingots and iron meteorites: Implications for the NASA Psyche mission. *Journal of Geophysical Research*, 125(2), e05927. <https://doi.org/10.1029/2019JE005927>
- Marchis, F., Enriquez, J., Emery, J., Mueller, M., Baek, M., Pollock, J., et al. (2012). Multiple asteroid systems: Dimensions and thermal properties from Spitzer Space Telescope and ground-based observations. *Icarus*, 221(2), 1130–1161. <https://doi.org/10.1016/j.icarus.2012.09.013>
- Marchis, F., Jorda, L., Vernazza, P., Brož, M., Hanuš, J., Ferrais, M., et al. (2021). (216) Kleopatra, a low density critically rotating M-type asteroid. *Astronomy and Astrophysics*, 653, A57. <https://doi.org/10.1051/0004-6361/202140874>
- Masiero, J. R., Grav, T., Mainzer, A. K., Nugent, C. R., Bauer, J. M., Stevenson, R., & Sonnett, S. (2014). Main-belt asteroids with WISE/NEOWISE: Near-infrared albedos. *The Astrophysical Journal*, 791(2), 121. <https://doi.org/10.1088/0004-637X/791/2/121>
- Masiero, J. R., Mainzer, A. K., Bauer, J. M., Cutri, R. M., Grav, T., Kramer, E., et al. (2021). Asteroid diameters and albedos from NEOWISE reactivation mission years six and seven. *The Planetary Science Journal*, 2(4), 162. <https://doi.org/10.3847/PSJ/ac15fb>
- Masiero, J. R., Mainzer, A. K., Grav, T., Bauer, J. M., Cutri, R. M., Dailey, J., et al. (2011). Main belt asteroids with WISE/NEOWISE. I. Preliminary albedos and diameters. *The Astrophysical Journal*, 741(2), 68. <https://doi.org/10.1088/0004-637X/741/2/68>
- Masiero, J. R., Mainzer, A. K., Grav, T., Bauer, J. M., Cutri, R. M., Nugent, C., & Cabrera, M. S. (2012). Preliminary analysis of WISE/NEOWISE 3-band cryogenic and post-cryogenic observations of main belt asteroids. *The Astrophysical Journal Letters*, 759(1), L8. <https://doi.org/10.1088/2041-8205/759/1/L8>
- Matsui, T., & Schultz, P. H. (1984). On the brittle-ductile behavior of iron meteorites: New experimental constraints. *Lunar and Planetary Science Conference Proceedings*, 89(S01), C323–C328. <https://doi.org/10.1029/JB089iS01p0C323>
- Matter, A., Delbo, M., Carry, B., & Ligi, S. (2013). Evidence of a metal-rich surface for the Asteroid (16) Psyche from interferometric observations in the thermal infrared. *Icarus*, 226(1), 419–427. <https://doi.org/10.1016/j.icarus.2013.06.004>
- McMullin, J. P., Waters, B., Schiebel, D., Young, W., & Golap, K. (2007). CASA architecture and Applications. In *Astronomical data analysis software and systems xvi*. In R. A. Shaw, F. Hill, & D. J. Bell (Eds.) (Vol. 376, p. 127). <https://ui.adsabs.harvard.edu/abs/2007ASPC..376..127M>
- Morbidelli, A., Bottke, W. F., Nesvorný, D., & Levison, H. F. (2009). Asteroids were born big. *Icarus*, 204(2), 558–573. <https://doi.org/10.1016/j.icarus.2009.07.011>
- Mueller, M., Harris, A. W., & Delbo, M., & MIRS Team. (2005). AAS/Division for Planetary Sciences Meeting Abstracts. 21 Lutetia and other M-types: Their sizes, albedos, and thermal properties from new IRTF measurements. #37 (Vol. 37). <https://ui.adsabs.harvard.edu/abs/2005DPS....37.0702M>
- Muhleman, D. O. (1972). Microwave emission from the Moon. *Progress in Astronautics and Aeronautics*, 28, 51–81.
- Muhleman, D. O., & Berge, G. L. (1991). Observations of Mars, Uranus, Neptune, Io, Europa, Ganymede, and Callisto at a wavelength of 2.66 mm. *Icarus*, 92(2), 263–272. [https://doi.org/10.1016/0019-1035\(91\)90050-4](https://doi.org/10.1016/0019-1035(91)90050-4)
- Neeley, J. R., Clark, B. E., Ockert-Bell, M. E., Shepard, M. K., Conklin, J., Cloutis, E. A., et al. (2014). The composition of M-type asteroids II: Synthesis of spectroscopic and radar observations. *Icarus*, 238, 37–50. <https://doi.org/10.1016/j.icarus.2014.05.008>

- Ockert-Bell, M. E., Clark, B. E., Shepard, M. K., Isaacs, R. A., Cloutis, E. A., Fornasier, S., & Bus, S. J. (2010). The composition of M-type asteroids: Synthesis of spectroscopic and radar observations. *Icarus*, 210(2), 674–692. <https://doi.org/10.1016/j.icarus.2010.08.002>
- Okada, T., Fukuhara, T., Tanaka, S., Taguchi, M., Arai, T., Senshu, H., et al. (2020). Highly porous nature of a primitive asteroid revealed by thermal imaging. *Nature*, 579(7800), 518–522. <https://doi.org/10.1038/s41586-020-2102-6>
- Ostro, S. J., Campbell, D. B., & Shapiro, I. I. (1985). Main-belt asteroids: Dual-polarization radar observations. *Science*, 229(4712), 442–446. <https://doi.org/10.1126/science.229.4712.442>
- Palmer, E. M., Heggy, E., Capria, M. T., & Tosi, F. (2015). Dielectric properties of asteroid Vesta's surface as constrained by Dawn VIR observations. *Icarus*, 262, 93–101. <https://doi.org/10.1016/j.icarus.2015.08.031>
- Parkhomenko, E. I. E. I. (1967). *Electrical properties of rocks*. Plenum Press.
- Piddington, J. H., & Minnett, H. C. (1949). Microwave thermal radiation from the Moon. *Australian Journal of Scientific Research A Physical Sciences*, 2(1), 63. <https://doi.org/10.1071/CH9490063>
- Pieters, C. M., Goswami, J. N., Clark, R. N., Annadurai, M., Boardman, J., Buratti, B., et al. (2009). Character and spatial distribution of OH/H₂O on the surface of the moon seen by M³ on Chandrayaan-1. *Science*, 326(5952), 568–572. <https://doi.org/10.1126/science.1178658>
- Podlowska-Gaca, E., Marciniak, A., Ali-Lagoa, V., Bartczak, P., Müller, T. G., Szakáts, R., et al. (2020). Physical parameters of selected Gaia mass asteroids. *Astronomy and Astrophysics*, 638, A11. <https://doi.org/10.1051/0004-6361/201936380>
- Raducan, S. D., Davison, T. M., & Collins, G. S. (2020). Morphological diversity of impact craters on asteroid (16) Psyche: Insight from numerical models. *Journal of Geophysical Research: Planets*, 125(9), e06466. <https://doi.org/10.1029/2020JE006466>
- Reddy, V., Le Corre, L., O'Brien, D. P., Nathues, A., Cloutis, E. A., Durda, D. D., et al. (2012). Delivery of dark material to Vesta via carbonaceous chondritic impacts. *Icarus*, 221(2), 544–559. <https://doi.org/10.1016/j.icarus.2012.08.011>
- Redman, R. O., Feldman, P. A., & Matthews, H. E. (1998). High-quality photometry of asteroids at millimeter and submillimeter wavelengths. *The Astronomical Journal*, 116(3), 1478–1490. <https://doi.org/10.1086/300495>
- Richardson, J. E., Melosh, H. J., Greenberg, R. J., & O'Brien, D. P. (2005). The global effects of impact-induced seismic activity on fractured asteroid surface morphology. *Icarus*, 179(2), 325–349. <https://doi.org/10.1016/j.icarus.2005.07.005>
- Rivkin, A., Howell, E., Lebofsky, L., Clark, B., & Britt, D. (2000). The nature of M-class asteroids from 3- μ m observations. *Icarus*, 145(2), 351–368. <https://doi.org/10.1006/icar.2000.6354>
- Rivkin, A. S., Clark, B. E., Ockert-Bell, M., Volquardsen, E., Howell, E. S., Bus, S. J., et al. (2011). Asteroid 21 Lutetia at 3 μ m: Observations with IRTF SpeX. *Icarus*, 216(1), 62–68. <https://doi.org/10.1016/j.icarus.2011.08.009>
- Rozitis, B. (2017). The surface roughness of (433) Eros as measured by thermal-infrared beaming. *Monthly Notices of the Royal Astronomical Society*, 464(1), 915–923. <https://doi.org/10.1093/mnras/stw2400>
- Rozitis, B., Ryan, A. J., Emery, J. P., Christensen, P. R., Hamilton, V. E., Simon, A. A., et al. (2020). Asteroid (101955) Benu's weak boulders and thermally anomalous equator. *Science Advances*, 6(41), eabc3699. <https://doi.org/10.1126/sciadv.abc3699>
- Sakatani, N., Ogawa, K., Arakawa, M., & Tanaka, S. (2018). Thermal conductivity of lunar regolith simulant JSC-1A under vacuum. *Icarus*, 309, 13–24. <https://doi.org/10.1016/j.icarus.2018.02.027>
- Sanchez, J. A., Reddy, V., Shepard, M. K., Thomas, C., Cloutis, E. A., Takir, D., et al. (2017). Detection of rotational spectral variation on the M-type Asteroid (16) Psyche. *The Astronomical Journal*, 153(1), 29. <https://doi.org/10.3847/1538-3881/153/1/29>
- Scott, E. R. D., Keil, K., Goldstein, J. I., Asphaug, E., Bottke, W. F., & Moskovitz, N. A. (2015). Early impact history and dynamical origin of differentiated meteorites and asteroids. In *Asteroids iv* (pp. 573–595). https://doi.org/10.2458/azu_uapress_9780816532131-ch030
- Shepard, M. K., Clark, B. E., Ockert-Bell, M., Nolan, M. C., Howell, E. S., Magri, C., et al. (2010). A radar survey of M- and X-class asteroids. II. Summary and synthesis. *Icarus*, 208(1), 221–237. <https://doi.org/10.1016/j.icarus.2010.01.017>
- Shepard, M. K., de Kleer, K., Cambioni, S., Taylor, P. A., Virkki, A. K., Rivera-Valentin, E. G., et al. (2021). Asteroid 16 Psyche: Shape, features, and global map. *The Planetary Science Journal*, 2(4), 125. <https://doi.org/10.3847/PSJ/abfdab>
- Shepard, M. K., Taylor, P. A., Nolan, M. C., Howell, E. S., Springmann, A., Giorgini, J. D., et al. (2015). A radar survey of M- and X-class asteroids. III. Insights into their composition, hydration state, & structure. *Icarus*, 245, 38–55. <https://doi.org/10.1016/j.icarus.2014.09.016>
- Shepard, M. K., Timerson, B., Scheeres, D. J., Benner, L. A. M., Giorgini, J. D., Howell, E. S., et al. (2018). A revised shape model of asteroid (216) Kleopatra. *Icarus*, 311, 197–209. <https://doi.org/10.1016/j.icarus.2018.04.002>
- Sierks, H., Lamy, P., Barbieri, C., Koschny, D., Rickman, H., Rodrigo, R., et al. (2011). Images of asteroid 21 Lutetia: A remnant planetesimal from the early solar system. *Science*, 334(6055), 487–490. <https://doi.org/10.1126/science.1207325>
- Sullivan, C. B., & Kaszynski, A. A. (2019). PyVista: 3D plotting and mesh analysis through a streamlined interface for the Visualization toolkit (VTK). *Journal of Open Source Software*, 4(37), 1450. <https://doi.org/10.21105/joss.01450>
- Sunshine, J. M., Farnham, T. L., Feaga, L. M., Groussin, O., Merlin, F., Milliken, R. E., & A'Hearn, M. F. (2009). Temporal and spatial variability of lunar hydration as observed by the deep impact spacecraft. *Science*, 326(5952), 565–568. <https://doi.org/10.1126/science.1179788>
- Takir, D., & Emery, J. P. (2012). Outer main belt asteroids: Identification and distribution of four 3- μ m spectral groups. *Icarus*, 219(2), 641–654. <https://doi.org/10.1016/j.icarus.2012.02.022>
- Takir, D., Reddy, V., Sanchez, J. A., Shepard, M. K., & Emery, J. P. (2017). Detection of water and/or hydroxyl on asteroid (16) Psyche. *The Astronomical Journal*, 153(1), 31. <https://doi.org/10.3847/1538-3881/153/1/31>
- Tholen, D. J. (1984). *Asteroid taxonomy from cluster Analysis of photometry*. University of Arizona. (Unpublished doctoral dissertation).
- Trumbo, S. K., Brown, M. E., & Butler, B. J. (2018). ALMA thermal observations of Europa. *The Astronomical Journal*, 156(4), 161. <https://doi.org/10.3847/1538-3881/aada87>
- Ulich, B. L., Cogdell, J. R., Davis, J. H., & Calvert, T. A. (1974). Observations and analysis of lunar radio emission at 3.09 mm wavelength. *The Moon*, 10(2), 163–174. <https://doi.org/10.1007/BF00655717>
- Vernazza, P., Brunetto, R., Binzel, R. P., Perron, C., Fulvio, D., Strazzulla, G., & Fulchignoni, M. (2009). Plausible parent bodies for enstatite chondrites and mesosiderites: Implications for Lutetia's fly-by. *Icarus*, 202(2), 477–486. <https://doi.org/10.1016/j.icarus.2009.03.016>
- Viikinkoski, M., Vernazza, P., Hanuš, J., Le Coroller, H., Tazhenova, K., Carry, B., et al. (2018). (16) Psyche: A mesosiderite-like asteroid? *Astronomy and Astrophysics*, 619, L3. <https://doi.org/10.1051/0004-6361/201834091>
- Webster, J., William, J., & Johnston, K. J. (1989). On the Wavelength Dependence of Apparent Emissivity of Asteroid Microwave Emissions: Ceres and Vesta. *Publications of the Astronomical Society of the Pacific*, 101, 122. <https://doi.org/10.1086/132410>
- Webster, W. J., Johnston, K. J., Hobbs, R. W., Lamphear, E. S., Wade, C. M., Lowman, P. D., et al. (1988). The microwave spectrum of the asteroid Ceres. *The Astronomical Journal*, 95, 1263. <https://doi.org/10.1086/114722>
- Weiss, B. P., & Elkins-Tanton, L. T. (2013). Differentiated planetesimals and the parent bodies of chondrites. *Annual Review of Earth and Planetary Sciences*, 41(1), 529–560. <https://doi.org/10.1146/annurev-earth-040610-133520>
- Zheng, Y.-C., Chan, K. L., Tsang, K. T., Zhu, Y.-C., Hu, G. P., Blewett, D. T., & Neish, C. (2019). Analysis of Chang'E-2 brightness temperature data and production of high spatial resolution microwave maps of the Moon. *Icarus*, 319, 627–644. <https://doi.org/10.1016/j.icarus.2018.09.036>